

# Poisson's Ratio

-Tuning the Poisson's Ratio of Glasses with  
High-Pressure Treatment.

---

*10. semester*

Jens Rasmus Knudsen Damgaard

*Institute for Chemistry & Biotechnology*

*Aalborg University*

*The 10. January 2019*



Titel:

Poisson's Ratio  
-An simulation and experimental  
study

Tema:

MD-Simulation

Projektperiode:

10 Semesterprojekt(30ECTS),  
efterårssemesteret  
2018

Deltagere:

Jens Rasmus Knudsen Damgaard

Synopsis:



Vejledere:

Morten Mattrup Smedskjær

Oplagstal:

Sidetal:

Antal appendiks:

Afsluttet den 10-01-2019

*Rapportens indhold er frit tilgængeligt, men offentliggørelse (med kildeangivelse) må kun ske efter aftale med forfatterne.*



# Forord

---

The master thesis is written as a 30 ECTS project around experimental work combined with MD-simulations. For the calculations and data processing the programs Matlab and LAMMPS has been used as platforms. The MD-simulations has been done solely in the LAMMPS which is a widely used MD-simulation language in the glass science area. The bibliography is placed at the end of the report just before the appendix and uses the Harvard-method which places the name and release year in the text when a citation is used.

I would like to express my gratitude towards the kind and help-full people who has assisted me and made the whole process an exciting experience. Thanks to Kacper Januchta and Mikkel Sandfeld Bødker who helped me with the experimental part, Søren Strandskov Sørensen, Han Liu and Mathieu Bauchy with questions for the MD simulations and Morten Mattrup Smedskjær for his assistance and guidance as supervisor. I have been met with an open mind and heart in the discussions which has made the work more joy-full and inspiring.

Thanks.

---

Jens Rasmus Knudsen Damgaard



# Contents

---

<b>1</b>	<b>Introduction</b>	<b>1</b>
<b>2</b>	<b>Problemstatement</b>	<b>3</b>
<b>3</b>	<b>Theory</b>	<b>5</b>
3.1	Glass Formation . . . . .	5
3.1.1	Nucleation and Crystal Growth . . . . .	5
3.1.2	Critical Cooling Rate . . . . .	7
3.2	Glass Structure . . . . .	8
3.3	MD-Simulation . . . . .	8
3.3.1	Empirical potentials . . . . .	8
3.3.2	Cooling rate effect . . . . .	10
3.3.3	Simulation Size and Concentration Effects . . . . .	11
3.3.4	Validation of structure models . . . . .	11
3.4	The Stiffness matrix and appropriate approximations . . . . .	12
<b>4</b>	<b>Experimental And Simulation Procedure</b>	<b>17</b>
<b>5</b>	<b>Results</b>	<b>19</b>
5.1	Radial Distribution and Coordination Number . . . . .	19
5.1.1	The Average Interatomic Distances dependency on pressure . . . . .	20
5.1.2	The Coordination Numbers dependency on pressure . . . . .	24
5.2	Density, Elastic Moduli and Poisson's Ratio . . . . .	27
5.2.1	Simulation and Experimental data comparison . . . . .	27
5.2.2	The Density, Elastic Moduli and Poisson's Ratio dependency on Pressure . . . . .	28
<b>6</b>	<b>Discussion</b>	<b>35</b>
<b>7</b>	<b>Conclusion</b>	<b>39</b>
	<b>Bibliography</b>	<b>41</b>
<b>A</b>	<b>Tables</b>	<b>43</b>
A.1	RDF and CN . . . . .	43
A.2	Density, Stiffness matrix elements, Elastic Modulus and Poisson's Ratio . . . . .	44
A.3	LAMMPS Code . . . . .	45



# Introduction 1

---

Glasses are amorphous materials that exhibits a glass transition hereunder the Oxide glasses which have been used in many applications due to their unique optical, electronic, mechanical and bio-related properties but their brittle behavior limits their exploitation so the development of glasses that show plastic behavior would open up to new areas of application.

Multi-component oxide glasses are mostly brittle because they lack a stabilizing mechanism in the shear direction so there is a need to develop glasses which exhibits ductility. The Poisson's ratio( $\nu$ ) could be a tool to design ductile oxide glasses and is defined as the negative to the transverse strains divided by the longitudinal strain( $\nu = -\frac{\epsilon_x}{\epsilon_z}$  where the longitudinal direction is z).[Massobrio et al., 2015] [Greaves et al., 2011]

There is empirical evidence for the existence of a relationship between fracture energy ( $E_{frac}$ ) and Poisson's ratio that shows a sharp transition between brittle and ductile metallic and oxide glasses around  $\nu_{BTD} = 0.31 - 0.32$ . Because the fracture energy is hard to measure and the Poisson's ratio is easy to measure this could ease the designing of more ductile oxide glasses and has already been used with success on metallic glasses.[Greaves et al., 2011]

To increase the ductility it is necessary to increase the Poisson's ratio and this is possible either by the composition or packing density of the glass which will be the focus in the current work.[Shi et al., 2014] [Greaves et al., 2011]

If the Poisson's ratio has to increase the packing density has to increase. Applying pressure or changing composition can increase the packing density. If the change in composition leads to a lowering in the connectivity then the packing density will increase so adding modifiers that create non-bridging oxygens(NBO) is an option. The atomic packing density is affected by temperature and pressure so the structural effects are hard to observe. Most data is obtained at ambient conditions but the temperature influences the size of the Poisson's ratio and increases when the glass transition is approached. So the temperature must be accounted fore in the determination of the Poisson's ratio. If the increase in Poisson's ratio is steep then the glass is depolymerizing significantly and this is linked to the state of the liquid. If the liquid is fragile the material will have a steep assent in the Poisson's ratio and vice versa fore strong liquids.[Greaves et al., 2011]

It is shown that the pressure increases the atomic packing density and thereby the Poisson's ratio. Silica glass is between 0.15-0.19 and after high pressure treatment the ratio is increased to 0.25 at 10GPa and 0.33 above 30GPa.[Greaves et al., 2011]

The effect of pressure treatment will off course be higher when the bulk to shear modulus

ratio ( $B/G$ ) is lower because the material is easier compressed without too much shearing. So at low Poisson's ratio the densification through pressure treatment will have higher effect.[Greaves et al., 2011]

If the atomic packing density has to increase then the connectivity has to decrease in other words the cross-linking of the different units through bridging oxygens will have to decrease and a good measure for the cross-linking will be the mean coordination number for the network former. So the Poisson's ratio is expected to decrease with increasing coordination number for the cation. Therefore the mean coordination number for the cation is a good index for the development of the Poisson's ratio.[Greaves et al., 2011]

To evaluate the glass structure and the elastic behavior MD simulations along with experimental work is applied to the chosen composition.

There has been done a lot of MD simulation with LAMMPS in the glass science field and the capability of the simulations to reproduce reality relies heavily on the potential available for the given force field as well as the given force field model.[Bauchy, 2014]

Therefore it is important to validate the obtained structure from the MD simulation through an structural study already done because an experimental study of the structure of the glass is out of the scope of this project as well as developing a trust-able potential. Then the experimental and MD simulation parts is evaluated for the density, elastic modulus and the Poisson's ratio after confirming the parameterization of the force field.

The composition of the current work is  $(30 + x)CaO - 5ZrO_2 - (65 - x)SiO_2$  where  $x = 15 \wedge 20$  and the two samples will be referred to as respectively  $45Ca50Si$  and  $50Ca45Si$  in this report. The specific composition has been chosen due to the access of structural data hereunder the radial distribution function(RDF) and Coordination number(CN) which is used to verify that the simulation procedure is done correctly and furthermore no elastic modulus and Poisson's ratio has been obtained for this particular material. The reason to put in Zr is to alter the atomic packing density through the size which is in between the Ca and Si atoms. The problem is that the coordination number of Zr eventually is higher than for Si and will counteract the potential better packing of the glass. As shown the addition of Zr up to 5-10% gives the role of network former to Zr. The Ca atom is added to lower the connectivity and thereby the number of bridging oxygens in the glass leading to an increase in the number of  $Q_2$  units in the glass which could result in a high Poisson's ratio.[Barbieri et al., 2015] [Montorsi et al., 2002]

# Problemstatement 2

---

With this study, we investigate the possibility to obtain oxide glasses with high Poisson's ratio (above 0.32) using pressure treatment. We use a combination of experiments (glass melting, pressure treatment, and characterization) and MD simulations to investigate the structural origins of the pressure-driven changes in density, elastic moduli and Poisson's ratio.



# Theory 3

---

## 3.1 Glass Formation

### 3.1.1 Nucleation and Crystal Growth

The glass is an amorphous material so the crystallization process have to be avoided under the cooling procedure. If nuclei are present in the material a crystallization is invoked while cooling.

A nucleation process can be either homogeneous or heterogeneous respectively initiated in the bulk of a melt or surface of a crucible or impurities in the melt. The classical nucleation theory addresses the homogeneous process where the creation of nuclei throughout the bulk is equally probable.

The overall nucleation process is described by

$$I = Ae^{-\frac{W^* + \Delta G_D}{kT}} \quad (3.1)$$

where A is a constant,  $W^*$  and  $\Delta G_D$  are respectively thermodynamic and kinetic free energy barriers to nucleation, k is the Boltzmann constant and T is the absolute temperature (K). The thermodynamic free energy ( $W^*$ ) is the critical work needed to create a nucleus that is stable and do not re-dissolve into the melt.

The thermodynamic free energy is characterized by two contributions through

$$W = \frac{4}{3}\pi r^3 \Delta G_v + 4\pi r^2 \gamma \quad (3.2)$$

where the first term represents the change in volume free energy per unit volume and the second term the change in surface energy. The volume free energy below the melting temperature  $T_m$  is positive and the surface energy term is negative where the latter dominates at small radius giving a critical radius for stable nuclei formation found by the differential  $\frac{dW}{dr}$  giving

$$r^* = -\frac{2\gamma}{\Delta G_v} \quad (3.3)$$

giving the critical work as

$$W^* = \frac{16\pi}{3} \frac{\gamma^3}{\Delta G_v^2} \quad (3.4)$$

Besides the competition between the surface energy and free volume energy the diffusion contributes with a kinetic energy barrier where the diffusion could be described by

$$D = \left( \frac{kT\lambda^2}{h} \right) e^{-\frac{\Delta G_D}{kT}} \quad (3.5)$$

where  $\lambda$  is the atomic jump distance. The diffusion can also be linked to viscosity ( $\eta$ ) through Stokes- Einteins equation

$$D = \frac{kT}{3\pi\lambda\eta} \quad (3.6)$$

If equation 3.6 and 3.5 is substituted into equation 3.1 the overall process is found to be

$$I = \left( \frac{Ah}{3\pi\lambda^3\eta} \right) e^{-\frac{W^*}{kT}} \quad (3.7)$$

The heterogeneous nucleation rate is similar to the homogeneous just interchanging A and  $W^*$  with  $A_{het}$  and  $W_{het}^*$  for the heterogeneous process.

If the equation 3.7 is plotted against temperature in figure 3.1 then the shape is easily explained. The volume free energy  $\Delta G_v$  will be small just below the melting temperature  $T_m$  leading to a large critical radius which makes the creation of nuclei most unlikely. When the temperature decreases the volume free energy will increase and the critical radius will eventually become very small and the creation of nuclei will most likely happen. When the temperature decreases further then eventually the viscosity will start dominate and the nucleation rate starts declining approaching zero.

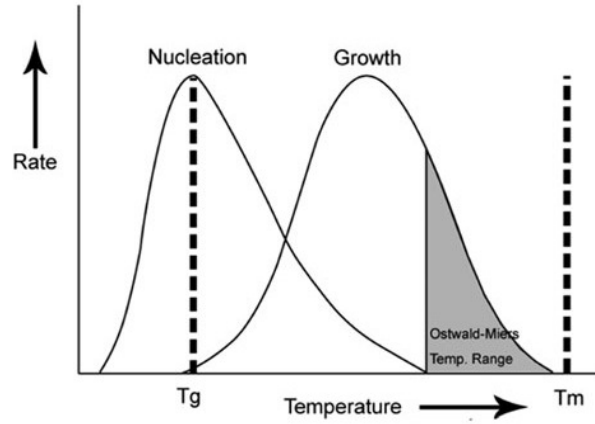


**Figure 3.1.** Effect of temperature on the rates of nucleation and crystal growth for a glass forming melt.

The crystall growth is described by

$$U = a_0\nu e^{-\frac{\Delta E}{kT}} (1 - e^{-\frac{\Delta G}{kT}}) \quad (3.8)$$

where  $a_0$  is the interatomic separation distance,  $\nu$  is the vibrational frequency,  $\Delta E$  and  $\Delta G$  are the kinetic and thermodynamic barriers to crystal growth. If the same approach as for the nucleation rate is used the following equation is obtained

$$U = \left( \frac{kT}{3\pi a_0^2 \eta} \right) (1 - e^{-\frac{\Delta G}{kT}}) \quad (3.9)$$

The nucleation and growth rate behave similar with the exception of the metastable undercooling zone that the nucleation exhibits. The growth rate starts increasing just below the melting temperature and decreases when the temperature gets low enough for the viscosity to dominate.

### 3.1.2 Critical Cooling Rate

If the process is considered isothermal then the volume fraction of crystals is described by

$$\frac{V_x}{V} = 1 - e\left(-\frac{\pi}{3}I_vU^3t^4\right) \quad (3.10)$$

where  $V_x$  is the volume of the crystals,  $V$  is the volume of the sample and  $t$  is the time the sample has been held at the experimental temperature.

When the volume fraction of crystals is plotted in a time-temperature diagram the curve is called a time-temperature-transformation(TTT) curve. The plot is shown in figure 3.2 for visualization.

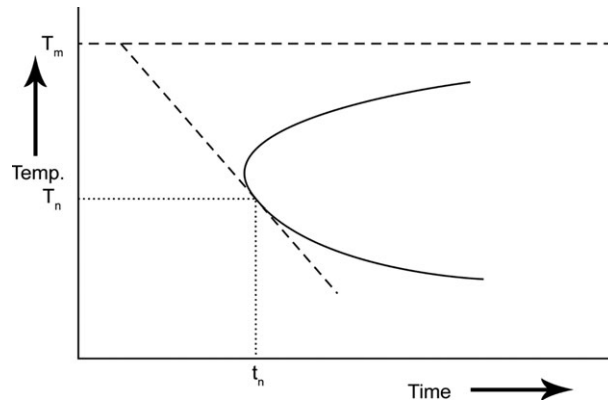


*Figure 3.2.* A time-temperature-transformation curve for a glass forming melt.

If the cooling rate needed to obtain the specific crystal volume fraction is calculated from the melting temperature and the time it takes to reach the nose of the TTT curve then the critical cooling rate is given by

$$\left(\frac{dT}{dt}\right)_c = \frac{T_m - T_n}{t_n} \quad (3.11)$$

where values below this critical cooling rate gives compositions with crystal volume fractions higher than the specification for a glass. So to produce glass the cooling rate needs to be the same or higher than the critical cooling rate.

The use of the TTT-curve and critical cooling rate is merely as a conceptual tool for understanding the glass transformation process because the curve has only been produced for a small number off compositions.

## 3.2 Glass Structure

### 3.3 MD-Simulation

MD simulations involve studying the movement of an assembly of atoms. First the initial positions is generated randomly either by a random number generator or from crystalline configurations followed by an equilibration at high temperatures for sufficiently long enough times that the atoms has lost their memory effects of the initial configuration leading to randomly placed atoms in the simulation box. The temperature normally used is between 5000-8000K for the melt and quench process. The quenching is done with cooling rates between 0.1K/ps and up to 10K/ps ensuring to freeze the liquid in an amorphous configuration. When the glass structure is obtained the glass has to reach an equilibrium for the chosen ensemble before any measurements of the obtained mechanical properties is possible.[Massobrio et al., 2015]

The initial velocities is generated from either an gaussian distribution or just a random number generator if the number of atoms is small to ensure conservation of the momentum. When the potential has been defined the forces on each atom can be calculated and now both position, velocity and force acting on each particle is known.

Then the configuration has to be moved forward in time and the algorithm used i LAMMPS is a verlet velocity and there are off course other algorithms that can be used.

After moving all the atoms forward in time all the positions, velocities and forces are updated at the same time. Now the procedure can be ran multiple times until the desired length of the simulation is reached.

During the simulation procedure it is necessary to employ a thermostat to ensure that the energy and hence the momentum is conserved so it is possible to reach an equilibrium for the given ensemble. This can be done in many ways but the most used one in LAMMPS is the Nose-Hover thermostat that uses an external heat bath to control temperature through momentum transfer from the heat bath into the simulation box at the boundaries.

The biggest advantage over other simulation procedure is that the possible size of the system to be simulated goes from a few hundred atoms to thousands or even millions of atoms.

The MD simulation on a multi-component oxide glass contains several challenges as transferable empirical potentials, cooling rate, system size, concentration effect on the simulated glass structures and validation of the structure models.

#### 3.3.1 Empirical potentials

Empirical potentials is widely used and the base of many MD simulations and recently empirical potentials applicable to multi-component glasses has been developed. The potential is the foundation of the simulation and as such is critical for the outcome. The validity and accuracy of the simulated structures depend on the quality of the potential and therefore the development of those potentials is important.

The potential consists of a long range columbic interaction and a short range interaction consisting of a repulsive term and a power attractive term to account for dispersion interactions which is expressed in the Buckingham potential and the total potential

function is

$$U_{ij}(r_{ij}) = \frac{q_i q_j}{4\pi\epsilon_0 r_{ij}} + A_{ij} \exp\left(-\frac{r}{\rho_{ij}}\right) - \frac{C_{ij}}{r^6} \quad (3.12)$$

where  $A$ ,  $\rho$  and  $C$  is parameters,  $r$  is the inter-atomic distance and  $q$  is the charge of atom  $i$  and  $j$ . Systems with a high temperature and unreasonable initial configurations of the atoms can overcome the potential barrier and fall into the potential well leading to "fusion" resulting in infinitely high energies of the system. To correct for this nonphysical behavior a separate potential function such as 12-18 Lennard-Jones potential or a spline function for shorter distances is added to the original Buckingham potential. The distance  $r_0$  at which the spline function is applied is defined as the  $r$  value at which the second derivative of the potential energy equals 0 and the parameters has to be fitted so the potential and the derivative of the potential is continuous at  $r_0$ . It is not necessary to do this in LAMMPS if the program is set up nicely with all the atoms at a large enough distance initially.[Massobrio et al., 2015]

There is several other potentials developed for multi-component glasses such as the Morse and Born-Mayer-Huggins with different parametrizations and charges assigned. The Born-Mayer-Huggins can be used with the Matsui, Jakse or Delaye parametrizations along with the partial charges for the Matsui and Jakse where the Delaye uses formal charges. Furthermore the Delaye potential includes an additional higher order dipolar dispersion two-body term. To constrain the bond angles of the network forming cations a three body interaction term can be added to correctly describe the structural unit geometry and bond angles between the structural units.[Bauchy, 2014]

The Morse potential with an additional term for short range repulsion has been developed as well as an morse potential with the hydrogen-oxygen interaction accounted fore. So there exists several potentials for multi-component glasses and they can be improved in several ways. The transferability is an issue because a parametrization of the oxygen-oxygen interaction can vary between different potentials and thereby other cation-anion interactions can not be mixed and used together. So a simultaneous fitting of the parameters for the different interactions from a large database is a way to make a unified potential that can be used as pleased.[Massobrio et al., 2015]

Most of the potentials is fitted under ambient pressure and temperature which is a problem when the glasses is subjected to high temperatures and pressures during the simulations so the need of potentials covering a larger range of temperatures and pressures is important.[Massobrio et al., 2015]

Glasses that shows coordination numbers dependent on composition gives rise to the need of developing coordination dependent potentials. An example is the boron anomaly which is associated with the boron coordination change as a function of temperature. The addition of up to 40% sodium oxide to boron oxide changes the coordination of the boron ions from 3 to 4 and adding more sodium oxide increases the number of non bridging oxygen's in the glass so the need of a potential that is dependent on the change in coordination number is obvious. The dependence on composition gets even trickier regarding borosilicate and boroaluminosilicate glasses. Several potentials have been developed around the mentioned cases but the development of better potentials for these mixed glass former glasses remain a major challenge in simulating mixed glass former glasses.[Massobrio et al., 2015]

Most of the early simulations used formal charges for the potentials whereas more recently

developed potentials use partial charge which turns out to reproduce the coordination and bond angles in glasses successfully when fine tuning of short range parameters is applied. Whether it is the partial or full charge potentials that are used it is based on a rigid ion model. It is possible to take polarization effects during the simulation into account through a core-shell model where the shells is allowed to either follow the particles during the simulation (dynamic shell model) or the shell position is adjusted or equilibrated after each simulation step. Applying the core-shell model prolong the simulation time but was found to reproduce the melt to glass transition during the cooling process by keeping certain  $Q_n$  species and silicon coordination defects for longer time.

If the simulation size is limited to a few hundred atoms and a length of tens of picoseconds then ab initio based molecular dynamics (AIMD) is a possibility and should be compatible with all glass systems due to the accurate first principles calculations as long as the chemical bonding is described well enough. The results from AIMD can be used as a validation tool for normal MD simulation potentials due to their accuracy.[Massobrio et al., 2015]

The current work is based on an empirical buckingham potential using full charge and a rigid ion core model.

### 3.3.2 Cooling rate effect

The cooling rate in MD simulations is due to the small timesteps (femtoseconds) which leads to a limitation in simulation length (hundreds of pico-seconds to a few nano-seconds) 6-9 orders of magnitude larger than the fastest experimental cooling rates. The huge difference between experimental and simulation cooling rates has been questioned and as the computational power has increased it has been possible to exploit the cooling rate effect on for example bioactive glasses like  $Na_2O - CaO - P_2O_5 - SiO_2$  showing a  $Q_n$  distribution for Si insensitive for the choice of cooling rates as long as it do not exceed 5-10K/ps and has a system size over 1000 atoms whereas the  $Q_n$  distribution of P is more sensitive to the cooling rate effect and decreasing the cooling rate leads to more phosphorus  $Q_0$  species. This result is confirmed from both NMR experiments and MD simulations with polarizable potentials implemented so to some extent the cooling rate effect is important.[Tilocca, 2013] [Massobrio et al., 2015]

The reason why a cooling rate much higher than the experimental ones can be used is that the size of the system is so much smaller than the real samples leading to a much faster equilibration of the system regarding the lowest possible energy state at a certain temperature.[Massobrio et al., 2015]

As mentioned above the melt quench process is normally used but for the current work the method used in a study for the composition chosen here used a step wise method which do not directly implement a specific cooling rate. The step wise procedure jumps from one state to another and equilibrates between the jumps so the cooling rate is the part of the equilibration at the new state where the thermostat regulates the temperature from the start temperature and down to the specified temperature at the current state. This leads to different cooling rates between successive jumps especially when the jumps is differently spaced.[Montorsi et al., 2002]

The cooling rate for the melt quench process in this study is 1K/ps as in the study by [Bauchy, 2014] where the role of the potential is studied. This cooling rate is well below

the upper critical value between 5-10K/ps so should avoid most of the cooling rate effect.

### 3.3.3 Simulation Size and Concentration Effects

The system size of simulated oxide glasses with today's computer power can be up to millions of atoms but to replicate the desired properties of many glass systems only a few thousands of atoms is necessary. There are certain features which cant be reproduced only with a few thousands of atoms for example the clustering of minor component rare earth ions in glasses. To simulate the clustering well enough a system size of more than 6000 atoms is necessary. When there is so low a content off rare earth ions and other components it has to be larger systems to make it statistically significant. [Tilocca, 2013] [Massobrio et al., 2015]

The simulation size in this study is chosen to be  $\approx 500$  and  $\approx 4000$  atoms to test the size effect. The problem should be expected to arise around the Zirconium because of the low amount of the species in the glass structure only 5% in mole.

### 3.3.4 Validation of structure models

To validate the structure obtained from simulations it is possible to determine the total pair distribution function (PDF)  $g(r)$  from X-ray or neutron diffraction and compare with the calculated total PDF from the simulation. When the two total PDF's has to be compared a total deviation can be calculated by the  $R_x$  defined as the sum of squared errors divided by the sum of the experimental values

$$R_x = \frac{\sum_{i=1}^N (g(r) - g_{exp}(r))^2}{\sum_{i=1}^N (g_{exp}(r))^2} \quad (3.13)$$

where the index exp indicates experiment. This has been commonly used and if the value is below 9% regarded as good agreement between simulation and experiment. The reason to use the total PDF is the complexity of the deconvolution into the partial PDF's because they are highly overlapped in the experiment.[Bauchy, 2014]

The composition  $(30 + x)CaO - 5ZrO_2 - (65 - x)SiO_2$  consists of 4 different elements and thereby there are 10 different partial PDF's which are highly overlapping for Si-Zr, Si-Ca, Ca-Ca, Zr-Ca and Zr-Zr partial PDF's with the bonding length evaluated to be in the range 3,47-3,70 a relatively narrow range for the 5 specified interactions. In the simulation part it is easy to evaluate the partial PDF's and thereby also the total PDF. [Montorsi et al., 2002]

The partial PDF is calculated from the measured structure factor  $S_{ij}(q)$  as

$$g_{ij}(r) = 1 + \frac{1}{2\pi^2 r \rho_0} \int_0^{\text{inf}} (S_{ij}(q) - 1) \sin(qr) dq \quad (3.14)$$

where  $S_{ij}(q) = \frac{I(q)}{N_A |f(q)|^2}$  and  $I(q)$  is the scattering intensity,  $f(q)$  is the atomic form factor for a given atom and  $q$  is the wave vector transfer of the projectile,  $N_A$  is the number of atoms and  $\rho_0$  is the average atomic density. The PDF  $g(r)$  gives the probability of finding an atom a distance  $r$  away from a given atom. Therefore the probability of finding an atom closer than the atomic radius is extremely small due to the interatomic repulsion and for large  $r$  the  $g(r)$  approaches a constant if there is no long range order. Furthermore if there is any peaks it indicates the most popular distances or in other words the mean

equilibrium distance between the two atoms.[Massobrio et al., 2015] [Bauchy, 2014]  
 To calculate the total PDF from the partial PDF's shown above in real space the sum

$$g(r) = \left( \sum_{i,j=1}^N c_i c_j b_i b_j \right)^{-1} \sum_{i,j=1}^N c_i c_j b_i b_j g_{ij}(r) \quad (3.15)$$

where  $c_i$  is the fraction of  $i$  atoms and  $b_i$  is the neutron scattering length of the species. Beside X-ray and neutron diffraction experiments NMR, EXAFS and Raman spectroscopy can give additional structural information for example NMR results provide besides the distribution of  $Q_n$  also information about how the cells are linked together.[Massobrio et al., 2015] [Bauchy, 2014]

In the present study the experimental structure data is obtained from others work and the simulation is only used to resolve the partial PDF's because there is no data on the total PDF.[Montorsi et al., 2002]

### 3.4 The Stiffness matrix and appropriate approximations

The stress strain relation can be found by applying the hooks law and the conservation of torque (the rotational analogue of newtons second law) to a small volume element of a bulk material. There are nine stress components for the six planes

$$\bar{\sigma} = \begin{bmatrix} \sigma_1 & \sigma_4 & \sigma_5 \\ \sigma_7 & \sigma_2 & \sigma_6 \\ \sigma_8 & \sigma_9 & \sigma_3 \end{bmatrix} \quad (3.16)$$

where

$$1 = xx \quad 2 = yy \quad 3 = zz \quad 4 = xy \quad 5 = xz \quad 6 = yz \quad 7 = yx \quad 8 = zx \quad 9 = zy \quad (3.17)$$

is used to mark the directions. The first and second index indicates respectively the direction of the normal to the plane and the applied external force. There are 3 normal and 6 shear stresses where the 6 shear stresses reduce to 3 due to zero rotation and the conservation of torque leading to

$$\bar{\sigma} = \begin{bmatrix} \sigma_1 & \sigma_4 & \sigma_5 \\ \sigma_4 & \sigma_2 & \sigma_6 \\ \sigma_5 & \sigma_6 & \sigma_3 \end{bmatrix} \quad (3.18)$$

where

$$4 = 7 = xy \quad 5 = 8 = xz \quad 6 = 9 = yz \quad (3.19)$$

and the notation of the index is defined similarly to the stress when considering the strain. Due to geometric symmetries the 9 strain components reduce to 6 strain components assembled in the matrix

$$\bar{e} = \begin{bmatrix} e_1 & e_4 & e_5 \\ e_4 & e_2 & e_6 \\ e_5 & e_6 & e_3 \end{bmatrix} \quad (3.20)$$

where

$$4 = 7 = xy \quad 5 = 8 = xz \quad 6 = 9 = yz \quad (3.21)$$

and the generalized version of Hooke's law with the notation used above is

$$\begin{bmatrix} \sigma_1 \\ \sigma_2 \\ \sigma_3 \\ \sigma_4 \\ \sigma_5 \\ \sigma_6 \end{bmatrix} = \begin{bmatrix} C_{11} & C_{12} & C_{13} & C_{14} & C_{15} & C_{16} \\ C_{21} & C_{22} & C_{23} & C_{24} & C_{25} & C_{26} \\ C_{31} & C_{32} & C_{33} & C_{34} & C_{35} & C_{36} \\ C_{41} & C_{42} & C_{43} & C_{44} & C_{45} & C_{46} \\ C_{51} & C_{52} & C_{53} & C_{54} & C_{55} & C_{56} \\ C_{61} & C_{62} & C_{63} & C_{64} & C_{65} & C_{66} \end{bmatrix} \begin{bmatrix} e_1 \\ e_2 \\ e_3 \\ e_4 \\ e_5 \\ e_6 \end{bmatrix} \quad (3.22)$$

and in short form

$$\boldsymbol{\sigma} = \bar{\mathbf{C}} \mathbf{e} \quad (3.23)$$

where the strain as a function of stress can be found from the compliance matrix  $\mathbf{S}$  which is simply the inverse of the stiffness matrix  $\mathbf{C}$  through

$$\begin{bmatrix} e_1 \\ e_2 \\ e_3 \\ e_4 \\ e_5 \\ e_6 \end{bmatrix} = \begin{bmatrix} S_{11} & S_{12} & S_{13} & S_{14} & S_{15} & S_{16} \\ S_{21} & S_{22} & S_{23} & S_{24} & S_{25} & S_{26} \\ S_{31} & S_{32} & S_{33} & S_{34} & S_{35} & S_{36} \\ S_{41} & S_{42} & S_{43} & S_{44} & S_{45} & S_{46} \\ S_{51} & S_{52} & S_{53} & S_{54} & S_{55} & S_{56} \\ S_{61} & S_{62} & S_{63} & S_{64} & S_{65} & S_{66} \end{bmatrix} \begin{bmatrix} \sigma_1 \\ \sigma_2 \\ \sigma_3 \\ \sigma_4 \\ \sigma_5 \\ \sigma_6 \end{bmatrix} \quad (3.24)$$

and in short form

$$\mathbf{e} = \bar{\mathbf{S}} \boldsymbol{\sigma} \quad (3.25)$$

where the equations are only applicable in the elastic domain because it is based on Hooke's law so only for sufficiently low enough applied strains or stresses. The stiffness matrix can be further reduced for different materials due to symmetries resulting in only 2 linearly independent coefficients for isotropic materials.

Analogously to evaluating the energy of a stretched spring the elastic energy of the crystal can be evaluated as

$$U = \frac{1}{2} \sum_{\lambda=1}^6 \sum_{\mu=1}^6 \tilde{C}_{\lambda\mu} e_\lambda e_\mu \quad (3.26)$$

and then the stress components can be found from the derivative of the potential energy with respect to the associated strain component. If the  $\sigma_{xx}$  direction is evaluated

$$\sigma_1 = \frac{\partial U}{\partial e_1} = \tilde{C}_{11} e_1 + \frac{1}{2} \sum_{\beta=2}^6 (\tilde{C}_{1\beta} + \tilde{C}_{\beta 1}) e_\beta \quad (3.27)$$

and if the coefficient  $\frac{1}{2}(\tilde{C}_{1\beta} + \tilde{C}_{\beta 1})$  is compared with equation 3.22 it is seen that

$$C_{\alpha\beta} = \frac{1}{2}(\tilde{C}_{\alpha\beta} + \tilde{C}_{\beta\alpha}) = C_{\beta\alpha} \quad (3.28)$$

and thereby the 36 elements reduce to a maximum of 21 independent elements.

If it is a cubic crystal the elastic potential energy can be found with equation 3.26 to be

$$U = \frac{1}{2}C_{11}(e_1^2 + e_2^2 + e_3^2) + \frac{1}{2}C_{44}(e_4^2 + e_5^2 + e_6^2) + C_{12}(e_2e_3 + e_3e_1 + e_1e_2) \quad (3.29)$$

where the terms

$$(e_1e_4 + \dots) \quad ; \quad (e_6e_5 + \dots) \quad ; \quad (e_1e_6 + \dots) \quad (3.30)$$

has been neglected due to the minimum symmetry requirement which is the existence of four three-fold rotation axes.

If the stress components is evaluated

$$\frac{\partial U}{\partial e_1} = C_{11}e_1 + C_{12}(e_2 + e_3) \quad (3.31)$$

$$\frac{\partial U}{\partial e_4} = C_{44}e_4 \quad (3.32)$$

and compared with equation 3.22 the following symmetries is obtained

$$C_{12} = C_{13} \quad ; \quad C_{14} = C_{15} = C_{16} = 0 \quad (3.33)$$

$$C_{66} = C_{44} \quad ; \quad C_{61} = C_{62} = C_{63} = C_{64} = C_{65} = 0 \quad (3.34)$$

and thereby the stiffness matrix for a cubic crystal can be written as

$$\begin{bmatrix} C_{11} & C_{12} & C_{12} & 0 & 0 & 0 \\ C_{12} & C_{11} & C_{12} & 0 & 0 & 0 \\ C_{12} & C_{12} & C_{11} & 0 & 0 & 0 \\ 0 & 0 & 0 & C_{44} & 0 & 0 \\ 0 & 0 & 0 & 0 & C_{44} & 0 \\ 0 & 0 & 0 & 0 & 0 & C_{44} \end{bmatrix} \quad (3.35)$$

where the relations between the compliance and stiffnessmatrix is found from evaluating the inverse of the stiffnessmatrix

$$C_{44} = \frac{1}{S_{44}}; \quad C_{11} - C_{12} = (S_{11} - S_{12})^{-1}; \quad C_{11} + 2C_{12} = (S_{11} + S_{12})^{-1} \quad (3.36)$$

If it is a cubic solid that is isotropic then

$$C_{44} = \frac{C_{11} - C_{12}}{2} \quad (3.37)$$

can be derived and reduces the number of independent elements to 2 for the stiffness matrix.

If the above relations between the compliance matrix and stiffness matrix in equation 3.36 is used the following relations for the elastic modulus and poisson ratio can be obtained

$$E = \frac{1}{S_{11}} = \frac{(C_{11} - C_{12})(C_{11} + 2C_{12})}{C_{11} + C_{12}} \quad (3.38)$$

$$G = C_{44} = \frac{C_{11} - C_{12}}{2} = \frac{1}{2(S_{11} - S_{12})} = \frac{E}{2(1 + \nu)} \quad (3.39)$$

$$B = \frac{C_{11} + 2C_{12}}{3} = \frac{E}{3(1 - 2\nu)} \quad (3.40)$$

$$\nu = -\frac{S_{12}}{S_{11}} = \frac{C_{12}}{C_{11} + C_{12}} = \frac{E}{2G} - 1 \quad (3.41)$$

In the simulation  $C_{11}$  and  $C_{44}$  is estimated and used to calculate  $C_{44}$  from the relation in equation 3.37 from which all off the elastic moduli and Poisson's ratio can be found with the use of equations 3.38, 3.39, 3.40 and 3.41 applied in the elastic regime off the glass. To determine the stiffness matrix experimentally the longitudinal and transverse velocities of elastic waves (sound waves) is measured from the localization of the echo signal and calculated with

$$C_{11} = v_l^2 \rho \quad ; \quad C_{44} = v_t^2 \rho \quad (3.42)$$

along with equation 3.37 and for isotropic materials the stiffness matrix elements is calculated with the same equations whether the orientation is  $\langle 100 \rangle$ ,  $\langle 110 \rangle$  and  $\langle 111 \rangle$ .



# Experimental And Simulation Procedure 4

The glass was produced from a batch that was thoroughly mixed before it was melted in an oven for 2 hours to ensure homogeneity at a temperature of 1550°C where the temperature was raised to 1575°C a couple of minutes to make it less viscous before pouring out the melt on a brass plate to quench it prior to annealing. The annealing was done at 800°C for both samples which has a measured  $T_g$  value of respectively 783,7°C and 802,1°C for 45Ca50Si and 50Ca45Si.

The density and elastic modulus is measured before and after pressure treatment at 1GPa around the measured  $T_g$  values.

The Simulation design for the two different compositions is provided in table 4.1 and is the same for both glasses. The two glasses are treated through the stepwise and melt-quench methods with two different counts of atoms and at four different pressures respectively 1atm, 1GPa, 10GPa and 100GPa before further treatment.

Composition	45CaO - 5ZrO <sub>2</sub> - 50SiO <sub>2</sub>								50CaO - 5ZrO <sub>2</sub> - 45SiO <sub>2</sub>							
Method	Stepwise								Quenching							
Number of Atoms	4080 (4000)				510 (500)				4080 (4000)				510 (500)			
Pressure	1atm	1GPa	10GPa	100GPa	1atm	1GPa	10GPa	100GPa	1atm	1GPa	10GPa	100GPa	1atm	1GPa	10GPa	100GPa

**Table 4.1.** overview

The initial structure for all the glasses is obtained with a random positioning of the distribution of atoms in a large volume to avoid overlapping of the atoms followed by an energy minimization of the conjugate gradient (cg) algorithm in the Polak-Ribiere version to avoid too high potentials and combined with a relaxment off the pressure during the energy minimization down to a specified target.

The Stepwise procedure is done with NVT ensembles starting at 12000K and stepping down by 2000K until 6000K is reached and then an NPT ensemble is used for 3000K, 1500K and 300K (with an additional NVT at 3000K for the pressure treatments at 1, 10 and 100GPa so the transition between the two states is more smooth avoiding the loss of atoms) where all the runs has a duration of 40ps. An overview is provided in table 4.2.

Stepwise			
1atm		1, 10 and 100GPa	
Temperature(K)	Ensemble	Temperature(K)	Ensemble
12000	NVT	12000	NVT
10000	NVT	10000	NVT
8000	NVT	8000	NVT
6000	NVT	6000	NVT
3000	NPT	3000	NVT
1500	NPT	3000	NPT
300	NPT	1500	NPT
		300	NPT

**Table 4.2.** Stepwise

To ensure that the structure is fully equilibrated at 300K the Stepwise procedure is followed by an additional NPT ensemble lasting 500ps where the density is averaged and the final structure is used to run an NVT ensemble for statistical averaging of the partial RDF's for 150ps.

The melt-quench procedure is done only in NPT ensembles starting at 3000K with a simulation length of 1ns before cooling down to 300K at a cooling rate of  $1 \frac{K}{ps}$  followed by an equilibration at 300K for 1ns.

The final glass structure obtained from respectively the Stepwise and melt-quench process is then cooled down with a cooling rate of  $1 \frac{K}{ps}$  in an NPT ensemble to practically 0K and 0Pa to estimate the moduli and do the tensile testing. An cg energy minimization is ran on the glass structure before the deformation procedure starts and is also applied between successive deformation steps. The total deformation is 50% with a scaling of 0,001 in the normal stress directions and a change in tilt of 0,1 in the shear stress directions between successive deformation steps.

The timestep used is 2fs and the cut off for short and long range interactions is respectively 8 and  $10\text{\AA}$ .

## 5.1 Radial Distribution and Coordination Number

The experimental data used for comparison is taken from the source [Montorsi et al., 2002] and listed in table A.1. The complete set of simulation results for respectively the composition  $45Ca50Si$  and  $50Ca45Si$  is listed in the tables A.2 and A.3 for the average interatomic distance and the CN both obtained from the RDF at the pressures 1atm, 1GPa, 10GPa and 100GPa.

The deviation between the simulation and experimentally determined RDF and CN values along with the average deviation is shown in table 5.1 and the most obvious problem is the reproduction of the RDF and CN for the Calcium which leads to respectively 11,4-12,2% and 24,1-27,2% in deviation.

On the contrary the total difference between the different methods and sizes is only 1,1% and the 3 best performing simulations involves Quenching on a small system ( $\approx 500$ atoms) and Stepwise on a large system ( $\approx 4000$ atoms) and the fourth and fifth best overall simulation is Quenching on a large system ( $\approx 4000$ atoms) where the top 5 only vary between 6,7-7,0%.

All of the average interatomic distances for both Ca-O and Si-O is under estimated. Furthermore only two values for the Zr-O is over estimated shown with red in table 5.1 indicating a systematic error at least for the Ca-O and Si-O.

The CN's is underestimated for Ca, overestimated for Si and the Zr is mixed with two values under estimated marked with green in table 5.1 again indicating a systematic error for at least Ca and Si.

		Average Interatomic Distance			Coordination Number			Total
		Ca-O	Si-O	Zr-O	Ca	Si	Zr	
45Ca50Si	Stepwise 4080Atoms	12.2	1.6	2.1	27.2	0.8	1.7	7.6
	Stepwise 510Atoms	11.8	1.7	0.6	26.2	2.0	4.5	7.8
	Quenching 4080Atoms	11.8	1.7	1.3	25.2	0.8	1.5	7.0
	Quenching 510Atoms	11.4	1.7	2.5	25.0	0.2	0.8	6.9
50Ca45Si	Stepwise 4000Atoms	11.9	1.8	1.7	24.6	1.5	0.2	6.9
	Stepwise 500Atoms	12.0	1.8	0.4	25.4	1.0	5.7	7.7
	Quenching 4000Atoms	11.8	1.8	1.0	25.2	0.8	1.5	7.0
	Quenching 500Atoms	11.8	1.7	1.8	24.1	0.8	0.2	6.7

**Table 5.1.** The deviation of the RDF and CN simulations from the experimental data given in respectively table A.2 and A.1 for the composition  $45CaO - 5ZrO_2 - 50SiO_2$  and  $50CaO - 5ZrO_2 - 45SiO_2$  at a pressure of  $1atm$  where the last column is the total deviation.

### 5.1.1 The Average Interatomic Distances dependency on pressure

The data for the average interatomic distances from table A.2 and A.3 is plotted as a function of pressure with a confidence level off 95% in the figures 5.1-5.6 for comparison. For the Ca-O in figure 5.1 and 5.2 respectively for a small and large system size ( $\approx 500$  or  $\approx 4000$ ) it is seen that the different methods and compositions do not reveal significantly different parameter values indicating that the precision in the simulation should be increased to confirm this observation. Looking into the trend in the figures there is probably an increase in the average interatomic distance from 1 atm up to 10GPa and then it drops far below the starting value at 1atm when a pressure of 100GPa is reached. For the Si-O in figure 5.3 and 5.4 respectively for a small and large system size ( $\approx 500$  or  $\approx 4000$ ) it is seen that the different methods and compositions do not reveal significantly different parameter values indicating that the precision in the simulation should be increased to confirm this observation. Looking into the trend in the figures there is probably no increase in the average interatomic distance from 1 atm up to 1GPa and from 1GPa and up to 100GPa the distance is increased significantly.

For the Zr-O in figure 5.5 and 5.6 respectively for a small and large system size ( $\approx 500$  or  $\approx 4000$ ) it is seen that the different methods and compositions for the large system has parameter values that do not differ significantly from each other except the Quenching of the 50Ca45Si at a pressure of 1GPa. Looking at the small system the different compositions and methods lead to parameter values that is more unevenly distributed and hard to see a trend from. Looking into the trend seen for the large system in figur 5.5 there is probably an increase in the average interatomic distance from 1 atm up to 10GPa and then it drops down to around the starting value at 1atm when a pressure of 100GPa is reached.

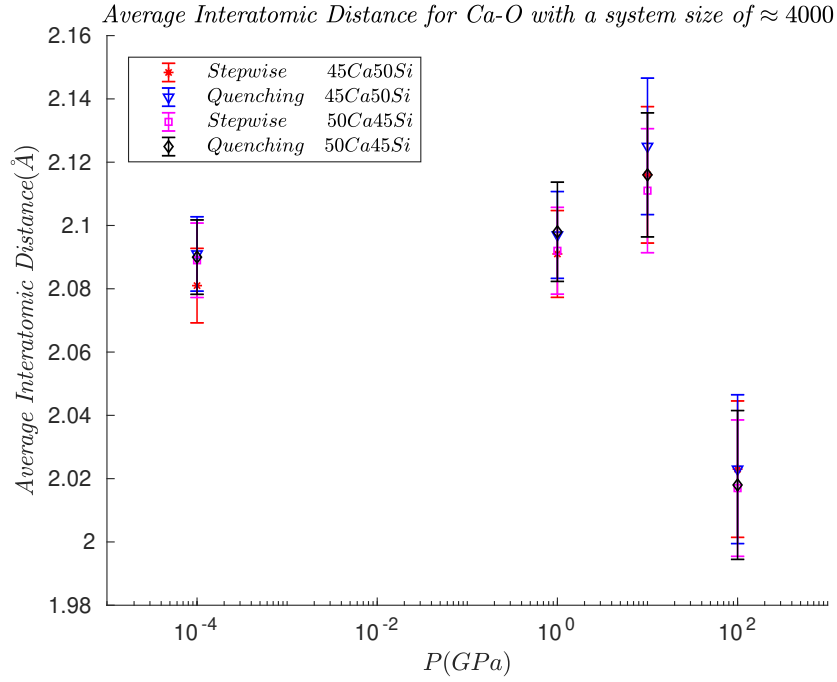


**Figure 5.1.** The Average Interatomic Distance plotted as a function of pressure with the 95% confidence intervals shown as vertical bars for a system size of respectively 4080 and 4000 for the two compositions and methods as indicated by the legends for the Ca-O bond length. The plot is scaled with a natural logarithm to improve the visual appearance.

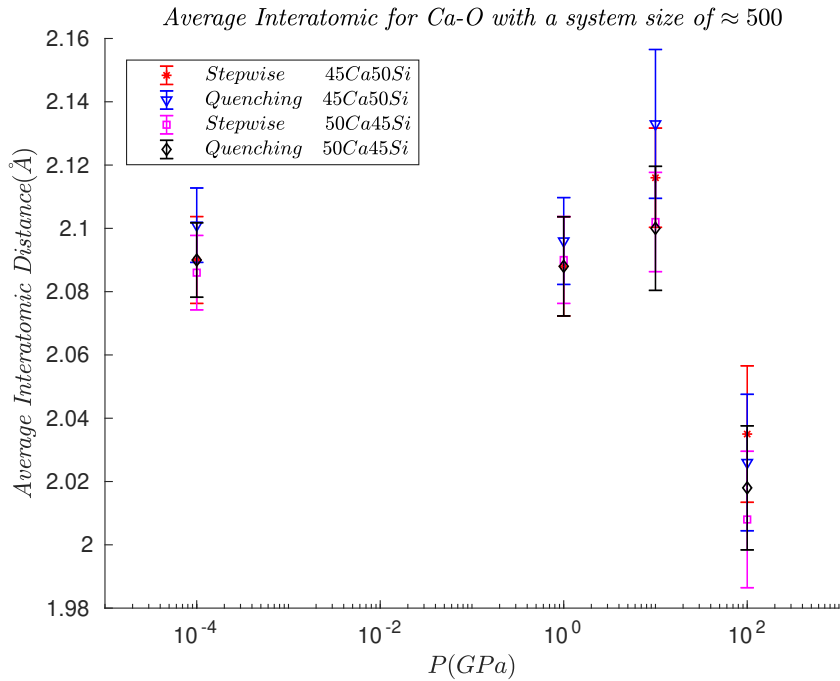


**Figure 5.2.** The Average Interatomic Distance plotted as a function of pressure with the 95% confidence intervals shown as vertical bars for a system size of respectively 510 and 500 for the two compositions and methods as indicated by the legends for the Ca-O bond length. The plot is scaled with a natural logarithm to improve the visual appearance.

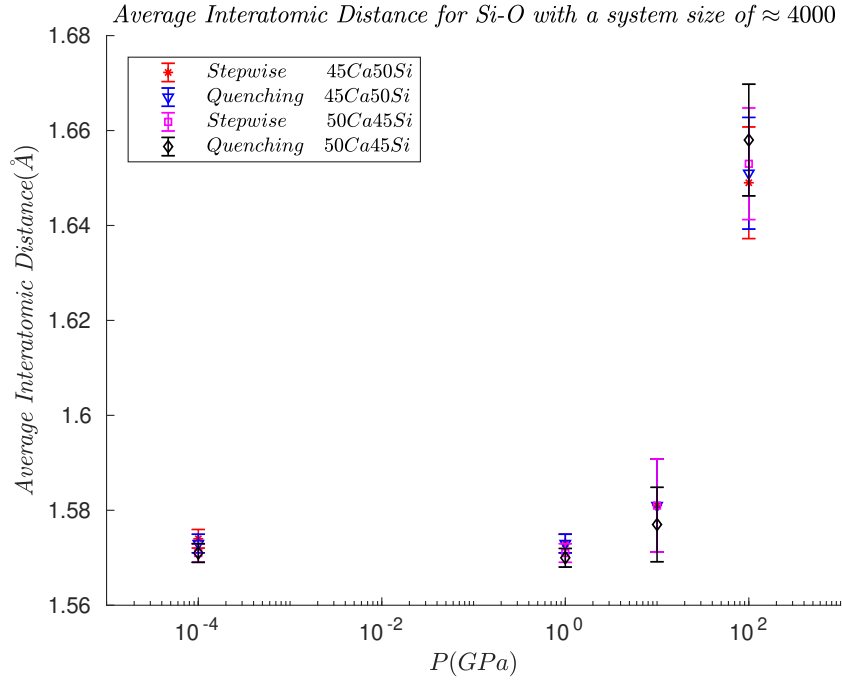


**Figure 5.3.** The Average Interatomic Distance plotted as a function of pressure with the 95% confidence intervals shown as vertical bars for a system size of respectively 4080 and 4000 for the two compositions and methods as indicated by the legends for the Si-O bond length. The plot is scaled with a natural logarithm to improve the visual appearance.

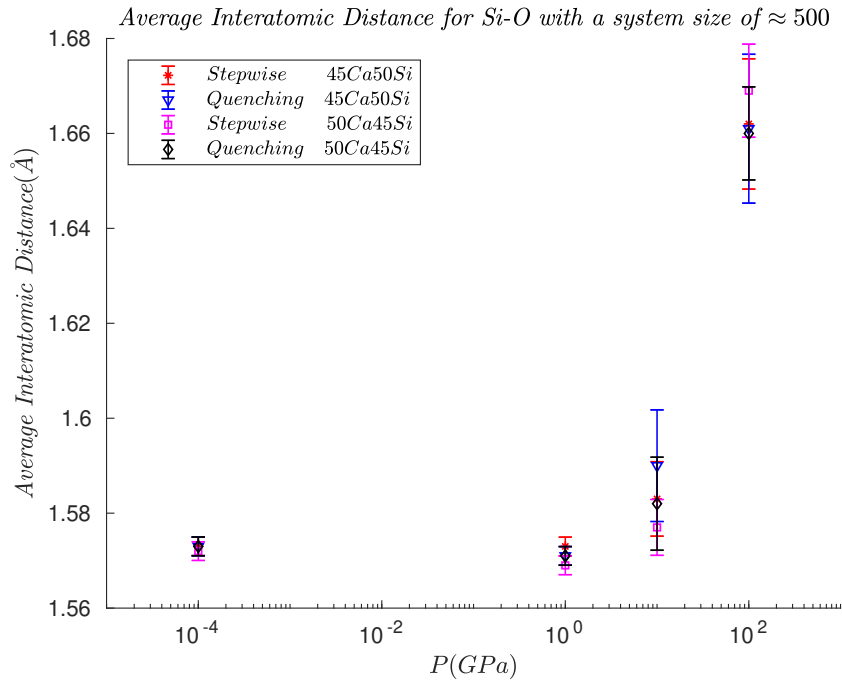


**Figure 5.4.** The Average Interatomic Distance plotted as a function of pressure with the 95% confidence intervals shown as vertical bars for a system size of respectively 510 and 500 for the two compositions and methods as indicated by the legends for the Si-O bond length. The plot is scaled with a natural logarithm to improve the visual appearance.

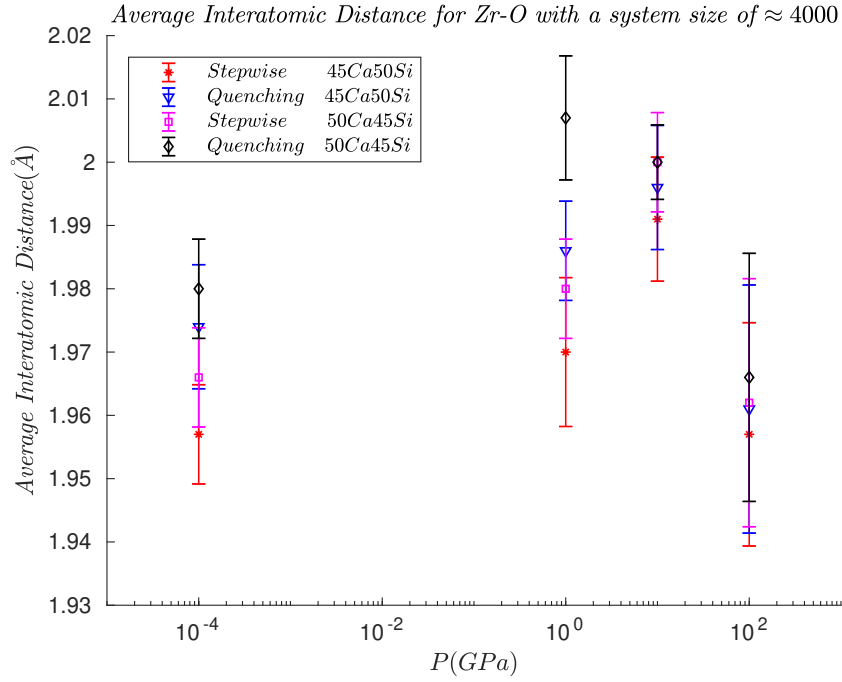


**Figure 5.5.** The Average Interatomic Distance plotted as a function of pressure with the 95% confidence intervals shown as vertical bars for a system size of respectively 4080 and 4000 for the two compositions and methods as indicated by the legends for the Zr-O bond length. The plot is scaled with a natural logarithm to improve the visual appearance.

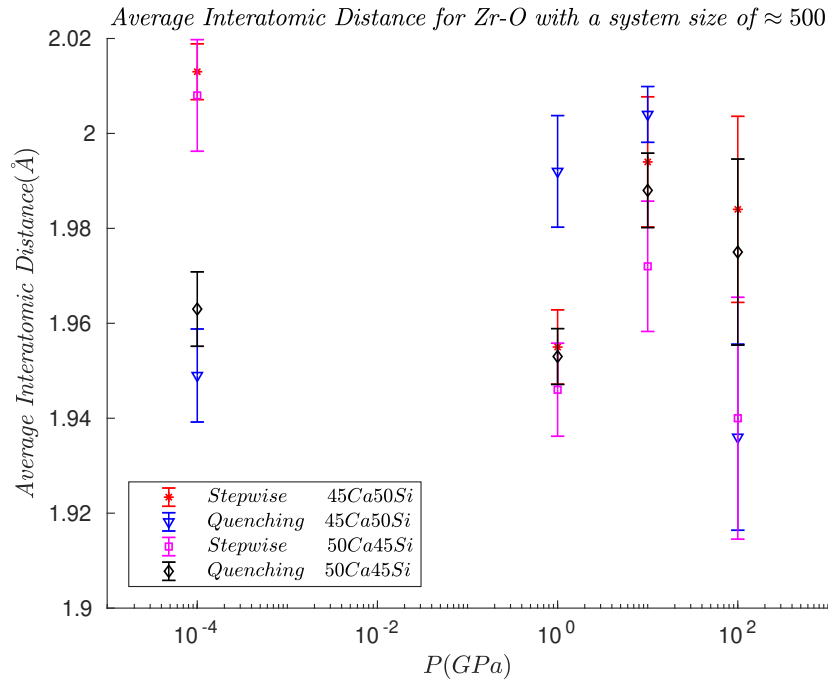


**Figure 5.6.** The Average Interatomic Distance plotted as a function of pressure with the 95% confidence intervals shown as vertical bars for a system size of respectively 510 and 500 for the two compositions and methods as indicated by the legends for the Zr-O bond length. The plot is scaled with a natural logarithm to improve the visual appearance.

### 5.1.2 The Coordination Numbers dependency on pressure

Due to the missing statistics on the CN's there is no confidence intervals plotted on any of the figures 5.7-5.12 showing the CN for the Ca, Si and Zr for the different systems. The difference between the large and small system size for Ca, Si and Zr coordination numbers is the way they are distributed at high pressures around 10GPa-100GPa where the small system shows greater dependency on the chosen method at elevated pressures. The CN for Zr in the large system in fig 5.11 shows higher dependency on the chosen method with respect to elevated pressures compared to Si and Ca in fig 5.9 and 5.7. For both Ca and Si in the figures 5.7-5.10 it is clear that their CN's increase non linear as a function of pressure going beyond respectively 7 and 5 fold coordination where the Ca actually get fairly close to a 8 fold coordination for a pressure of 100GPa. The Zr in fig 5.11 and 5.12 goes beyond a 5-7 fold coordination depending on the chosen method. The non linear increase in coordination number as a function of pressure might be present for Zr as well as for Ca and Si seen in fig 5.11 where only the blue triangle representing the Quenching of 45Ca50Si at 100GPa do not follow this trend. The trend of the CN for Zr in fig 5.12 for the small system deviates from the general trend of increasing CN with pressure.

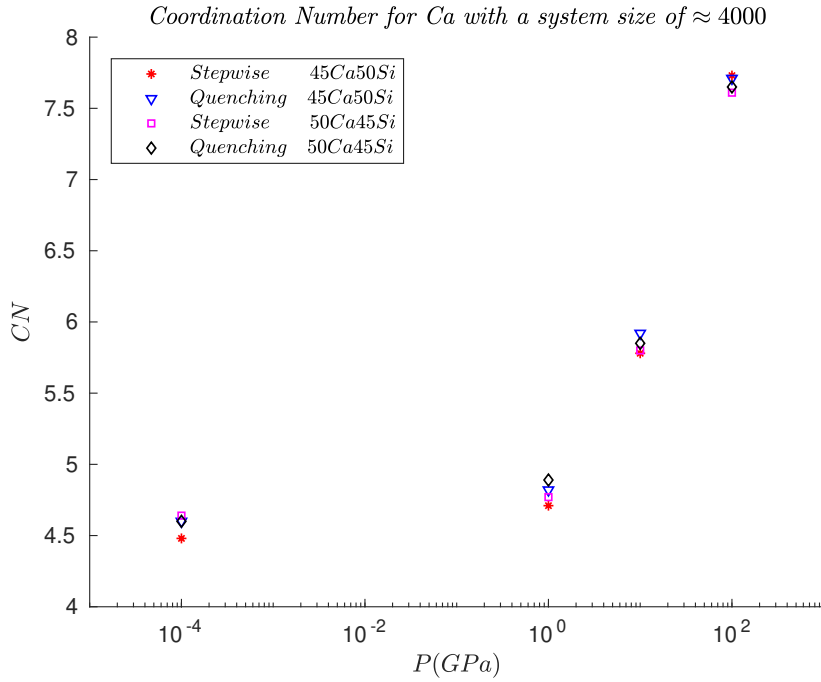


**Figure 5.7.** The Coordination Number for Ca plotted as a function of pressure for the two compositions 45Ca50Si and 50Ca45Si with respectively system sizes of 4080 and 4000 atoms with the quenching and stepwise methods indicated with the legends.

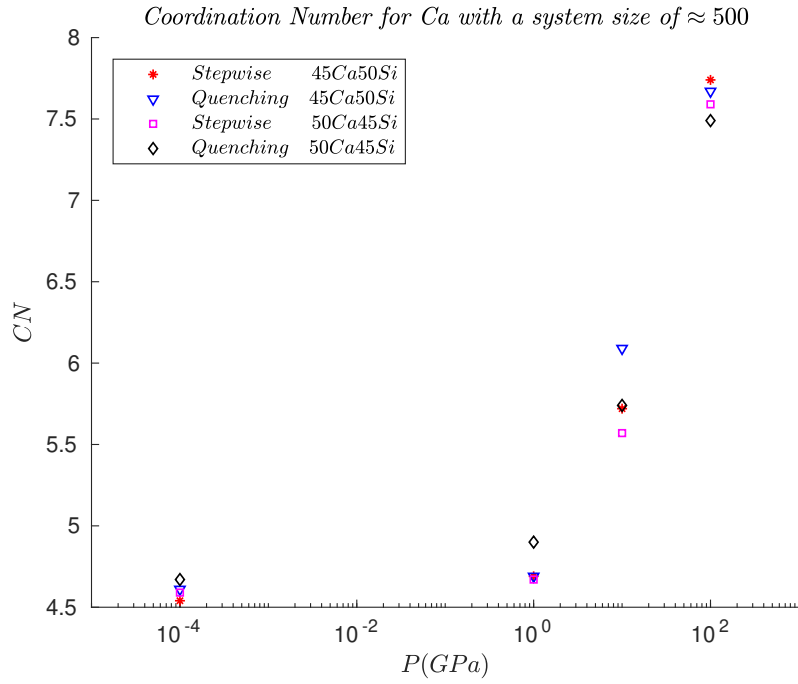


**Figure 5.8.** The Coordination Number for Ca plotted as a function of pressure for the two compositions 45Ca50Si and 50Ca45Si with respectively system sizes of 510 and 500 atoms with the quenching and stepwise methods indicated with the legends.

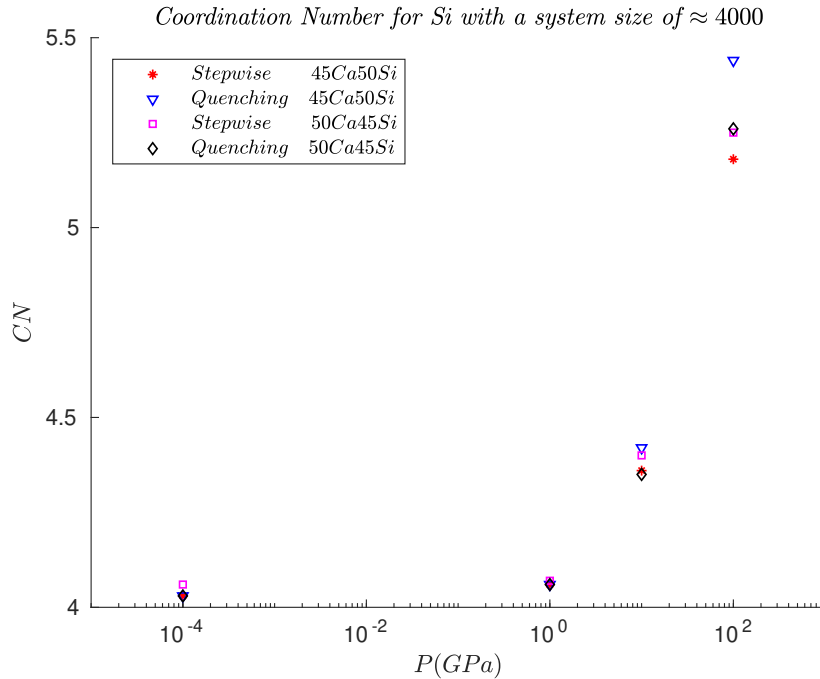


**Figure 5.9.** The Coordination Number for Si plotted as a function of pressure for the two compositions 45Ca50Si and 50Ca45Si with respectively system sizes of 4080 and 4000 atoms with the quenching and stepwise methods indicated with the legends.

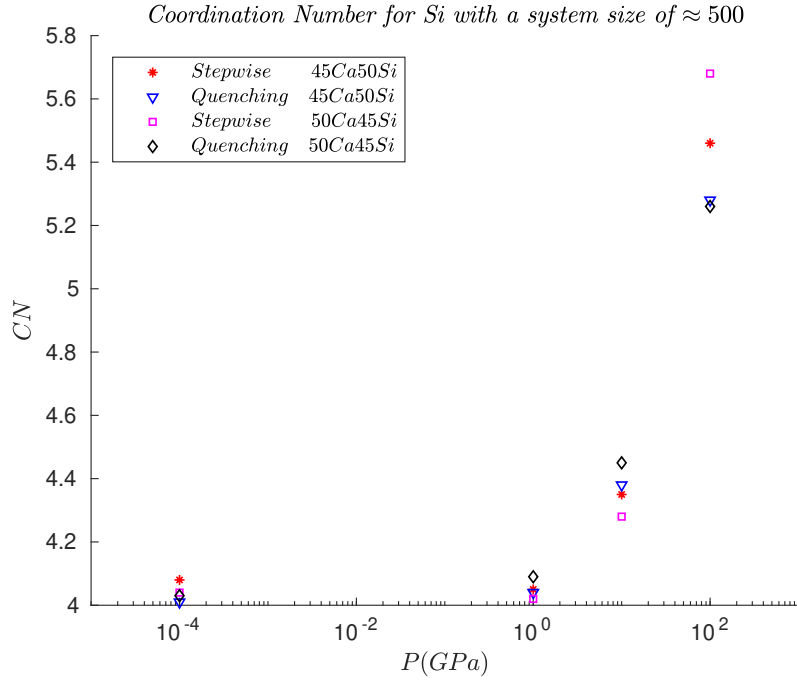


**Figure 5.10.** The Coordination Number for Si plotted as a function of pressure for the two compositions 45Ca50Si and 50Ca45Si with respectively system sizes of 510 and 500 atoms with the quenching and stepwise methods indicated with the legends.

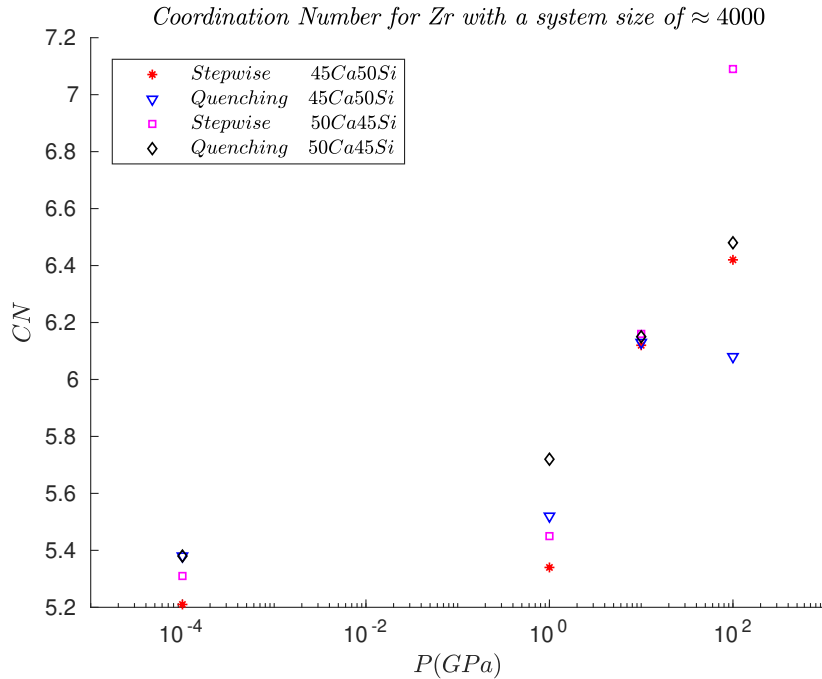


**Figure 5.11.** The Coordination Number for Zr plotted as a function of pressure for the two compositions 45Ca50Si and 50Ca45Si with respectively system sizes of 4080 and 4000 atoms with the quenching and stepwise methods indicated with the legends.

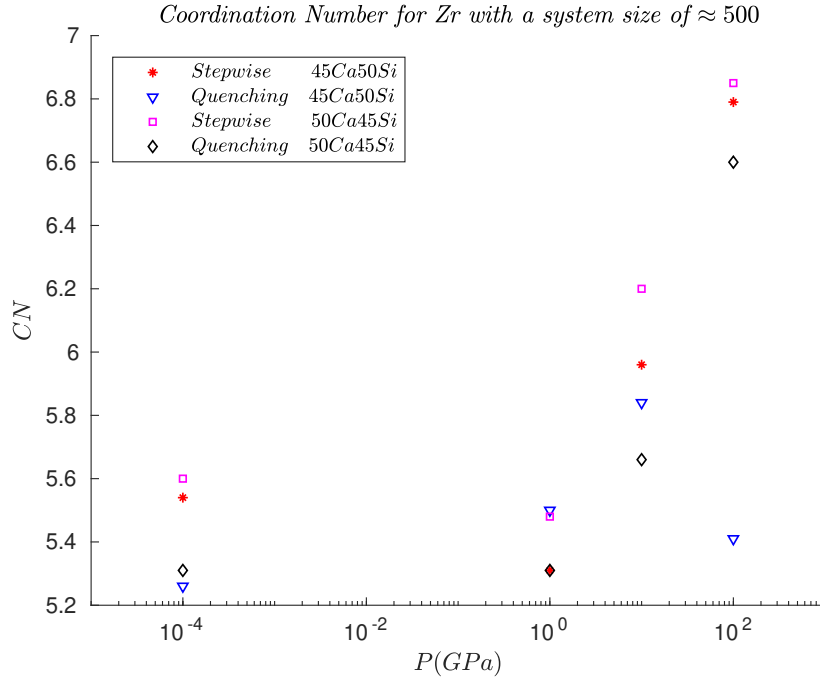


**Figure 5.12.** The Coordination Number for Zr plotted as a function of pressure for the two compositions 45Ca50Si and 50Ca45Si with respectively system sizes of 510 and 500 atoms with the quenching and stepwise methods indicated with the legends.

## 5.2 Density, Elastic Moduli and Poisson's Ratio

### 5.2.1 Simulation and Experimental data comparison

In table A.6 and A.7 the experimental data is shown along with the standard deviation. In table A.4 and A.5 the simulation data is shown along with the standard deviation. The average experimental values of  $\rho$ ,  $C_{11}$ ,  $C_{44}$ ,  $C_{12}$ , E, G, B and  $\nu$  is subtracted from the simulation data and the deviation in % is shown in the tables 5.2 and 5.3. In table 5.2 it is seen that all the stiffness matrix elements together with the elastic moduli is over estimated except for the Stepwise, 510Atoms at 1GPa where  $C_{12}$  and B is under estimated for the 45Ca50Si composition. Looking at the density it is mainly over estimated and the Poisson ratios is primarily under estimated with the Stepwise procedure for 4080Atoms showing the best agreement with experiment.

	Pressure	$\rho$	$C_{11}$	$C_{44}$	$C_{12}$	$E$	$G$	$B$	$\nu$	Total
Stepwise 4080 Atoms	1atm	2.7	7.5	8.9	5.2	8.4	8.9	6.6	1.5	6.2
	1GPa	2.8	17.9	27.0	3.3	24.3	27.0	11.7	9.4	15.4
Stepwise 510 Atoms	1atm	0.7	31.4	24.2	43.7	25.6	24.2	36.9	6.6	24.2
	1GPa	3.3	1.2	21.6	31.7	14.5	21.6	12.9	25.7	16.6
Quenching 4080 Atoms	1atm	0.1	26.1	29.0	21.4	28.1	29.0	24.2	2.9	20.1
	1GPa	4.9	23.1	30.9	10.9	28.7	30.9	18.0	7.6	19.4
Quenching 510 Atoms	1atm	1.3	27.9	20.3	40.8	21.8	20.3	33.6	6.91	21.6
	1GPa	2.5	24.9	15.3	40.8	17.3	15.3	31.8	9.1	19.6

**Table 5.2.** The deviation from experiment shown in % for density( $\rho$ ), stiffness matrix elements( $C_{11}$ ,  $C_{44}$  and  $C_{12}$ ), Youngs moduli( $E$ ), Shear moduli( $G$ ), Bulk moduli( $B$ ) and Poisson's ratio( $\nu$ ) for the different pressures (1atm and 1GPa), the composition  $45CaO-5ZrO_2-50SiO_2$  and different methods and system sizes. The red and black numbers is respectively under and over estimated.

In table 5.3 it is seen that all the density, stiffness matrix elements and the elastic moduli is over estimated except the  $C_{12}$  for the Stepwise procedure with 4080Atoms at 1GPa and the Quenching procedure with 510Atoms at 1atm where the latter also under estimates the bulk modulus. The poisson ratios is under estimated for all of the procedures except the Stepwise procedure with 510Atoms and both pressures. The best agreement with experiment is the Quenching procedure with 510Atoms sharply followed by the Stepwise procedure with 4080Atoms but all of the procedures reproduce reality equally well.

	Pressure	$\rho$	$C_{11}$	$C_{44}$	$C_{12}$	$E$	$G$	$B$	$\nu$	Total
Stepwise 4080 Atoms	1atm	1.4	19.5	31.8	1.3	28.3	31.8	11.5	11.5	17.1
	1GPa	5.8	17.2	33.9	9.2	28.8	33.9	5.7	17.3	19.0
Stepwise 510 Atoms	1atm	0.9	30.8	29.7	32.2	30.0	29.7	31.6	0.694	23.2
	1GPa	4.9	16.1	14.6	18.5	15.1	14.6	17.1	1.4	12.8
Quenching 4080 Atoms	1atm	0.8	27.4	39.8	9.0	36.5	39.8	19.2	10.8	22.9
	1GPa	6.9	32.9	38.1	24.3	36.8	38.1	29.2	4.7	26.4
Quenching 510 Atoms	1atm	2.0	6.2	22.0	16.8	17.3	22.0	4.1	16.7	13.4
	1GPa	5.5	26.8	30.8	20.5	29.7	30.8	24.1	3.6	21.5

**Table 5.3.** The deviation from experiment shown in % for density( $\rho$ ), stiffness matrix elements( $C_{11}$ ,  $C_{44}$  and  $C_{12}$ ), Youngs moduli( $E$ ), Shear moduli( $G$ ), Bulk moduli( $B$ ) and Poisson's ratio( $\nu$ ) for the different pressures (1atm and 1GPa), the composition  $50CaO-5ZrO_2-45SiO_2$  and different methods and system sizes. The red and black numbers is respectively under and over estimated.

## 5.2.2 The Density, Elastic Moduli and Poisson's Ratio dependency on Pressure

The density as a function of pressure is plotted in fig 5.13 and 5.14 for respectively the large and small system showing an non linear increase at elevated pressures. If a normal exponential function  $ae^{bP}$  where a and b are fitting parameters is fitted to the 8 different data sets it shows a nice correlation coefficient  $\approx 0.9$  for all data.

The density is determined with high enough accuracy to say that they are acutally different when comparing the different methods and compositions with each other and the

experimental data.

As the experimental data in tabel A.6 and A.7 shows the composition 50Ca45Si should have higher density at both 1atm and 1GPa with respect to the composition 45Ca50Si. The observation for the simulation data in the two figures 5.13 and 5.14 for both Stepwise and Quenching method has an identical trend.

Youngs moduli for a large system as plotted in figur 5.15 shows an increase from 1atm-10GPa and then it drops to a value above the values at 10GPa at a pressure of 100GPa. Again there is some overlap between the two compositions elastic modulus depending on the chosen method which can be avoided if the precision is enhanced.

For the small system in figure 5.16 the trend is less obvious because the different methods both remains the same, increase and decrease between 1atm and 1GPa whereas the increase and drop in modulus from 1GPa to 100GPa follows somewhat the same as in the large system. Furthermore it is observed that the Quenching procedure generates higher modulus than the Stepwise for the large system up to 10GPa.

Looking into the large and small systems for the shear modulus shown respectively in figure 5.17 and 5.18 it is found to follow the same trend and description as the Young's modulus except that there is no indications of a difference in the shear modulus due to a change from stepwise to quenching or vice versa.

The only trend to be observed from figure 5.19 for the large system is that the bulk modulus is increased when the Quenching method is used instead of the stepwise up to 10GPa and becomes identical at 100GPa. For the small system shown in figure 5.20 there is no obvious trend what so ever.

The poisson ratios shown in figure 5.22 for small system shows no clear definitive trend but looking into the poisson ratios in figure 5.21 for the large system indicates a trend where the ratio decreases from 1 atm and up to 10GPa. When 100GPa is reached there is no significant difference between the estimated poisson ratios within the 95% confidence level and depending on which one of the systems that is regarded the ratio either increases, decreases or stabilizes.

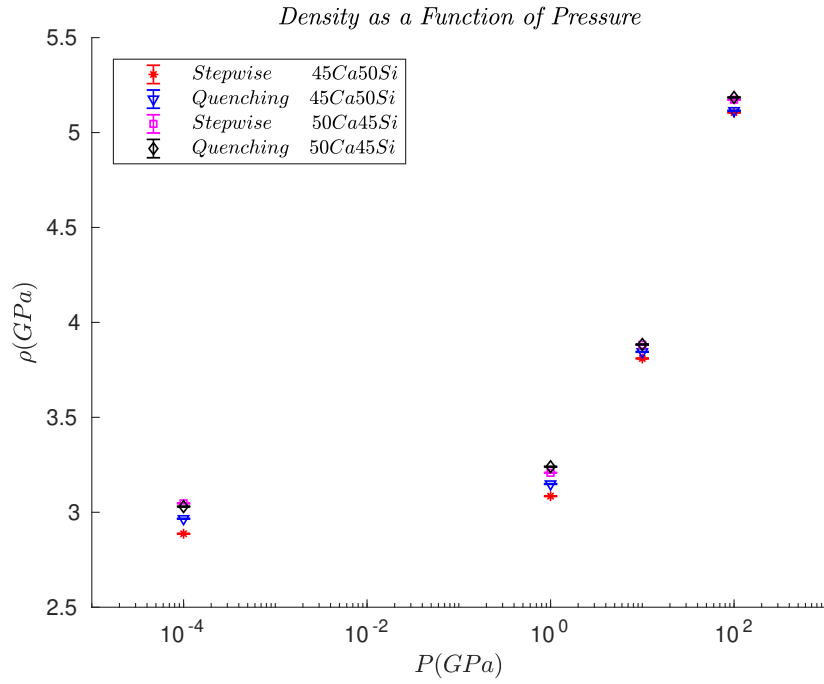


**Figure 5.13.** The density as a function of pressure along with 95% confidence intervals is shown for the large system size of  $\approx 4000atoms$  for the two simulation methods Stepwise and Quenching for both 45Ca50Si and 50Ca45Si as indicated by the legend.

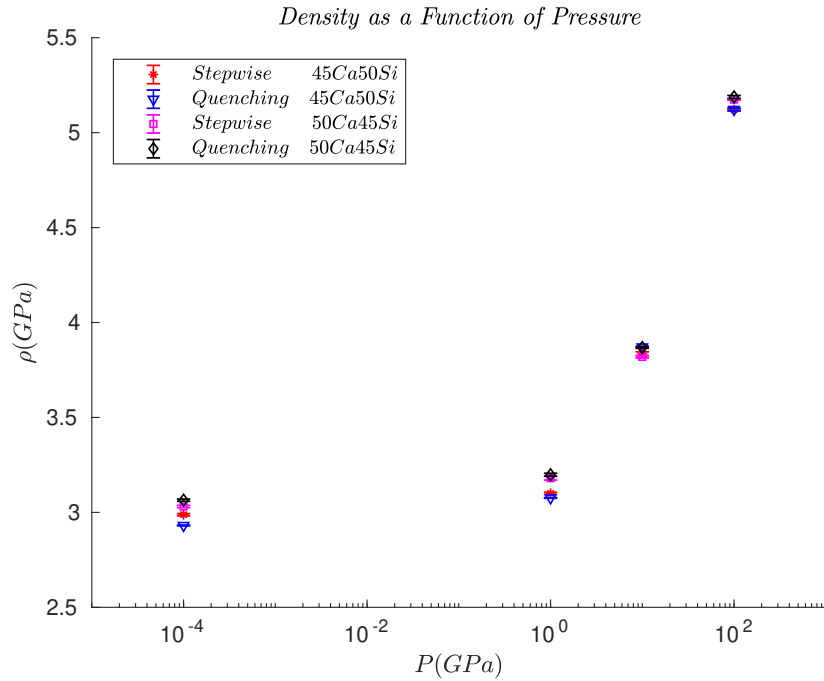


**Figure 5.14.** The density as a function of pressure along with 95% confidence intervals is shown for the small system size of  $\approx 500atoms$  for the two simulation methods Stepwise and Quenching for both 45Ca50Si and 50Ca45Si as indicated by the legend.

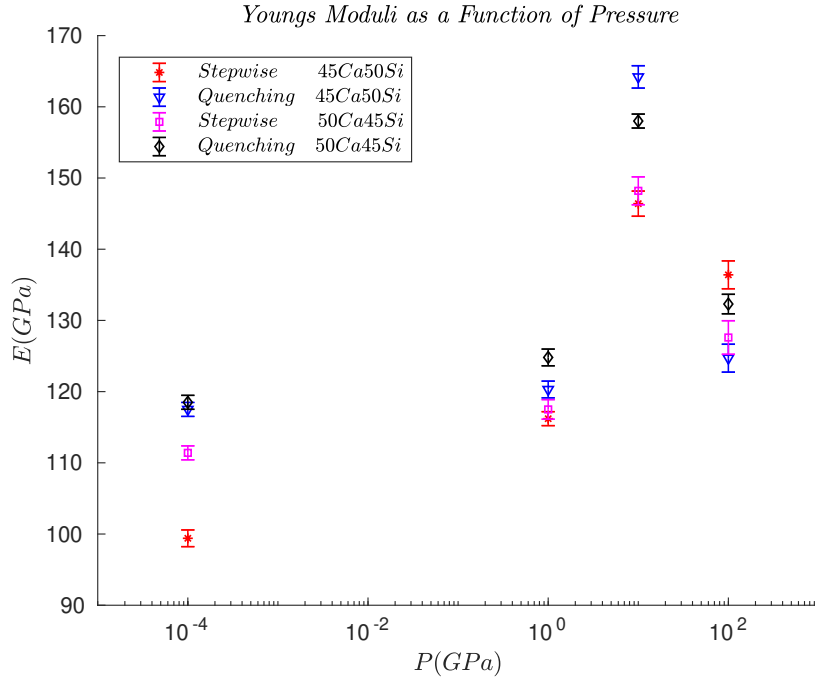


**Figure 5.15.** Young's modulus as a function of pressure along with 95% confidence intervals is shown for the large system size of  $\approx 4000atoms$  for the two simulation methods Stepwise and Quenching for both 45Ca50Si and 50Ca45Si as indicated by the legend.

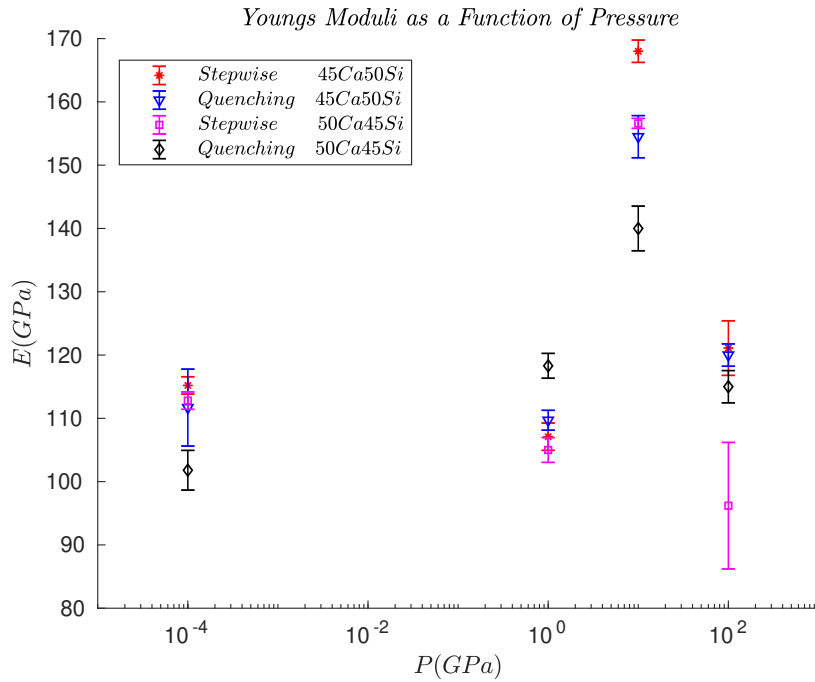


**Figure 5.16.** Young's modulus as a function of pressure along with 95% confidence intervals is shown for the small system size of  $\approx 500atoms$  for the two simulation methods Stepwise and Quenching for both 45Ca50Si and 50Ca45Si as indicated by the legend.

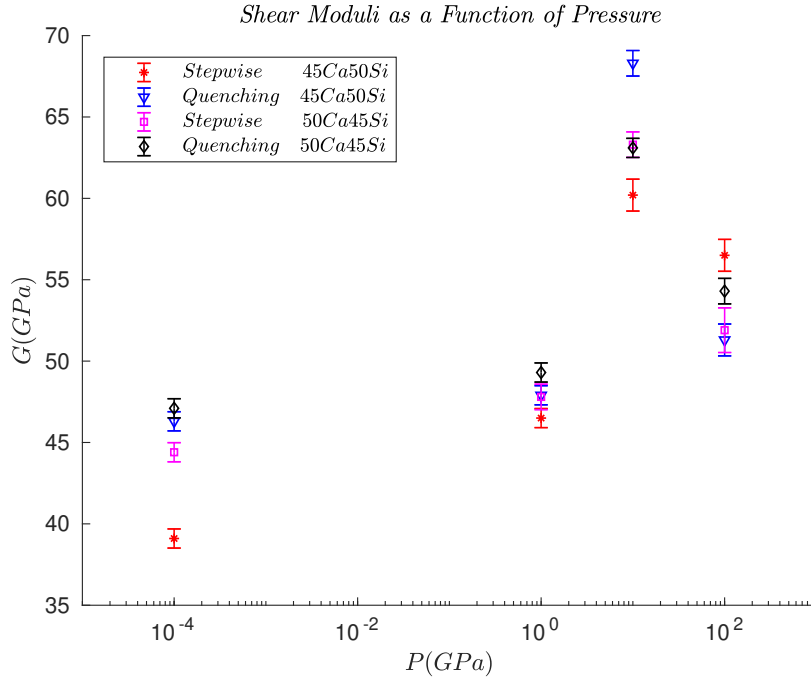


**Figure 5.17.** Shear modulus as a function of pressure along with 95% confidence intervals is shown for the large system size of  $\approx 4000atoms$  for the two simulation methods Stepwise and Quenching for both 45Ca50Si and 50Ca45Si as indicated by the legend.

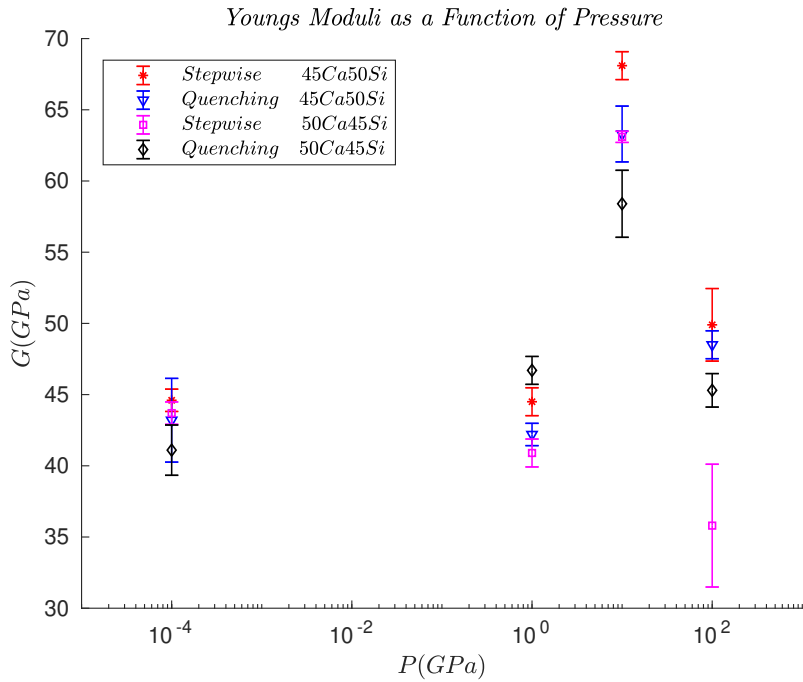


**Figure 5.18.** Shear modulus as a function of pressure along with 95% confidence intervals is shown for the small system size of  $\approx 500atoms$  for the two simulation methods Stepwise and Quenching for both 45Ca50Si and 50Ca45Si as indicated by the legend.

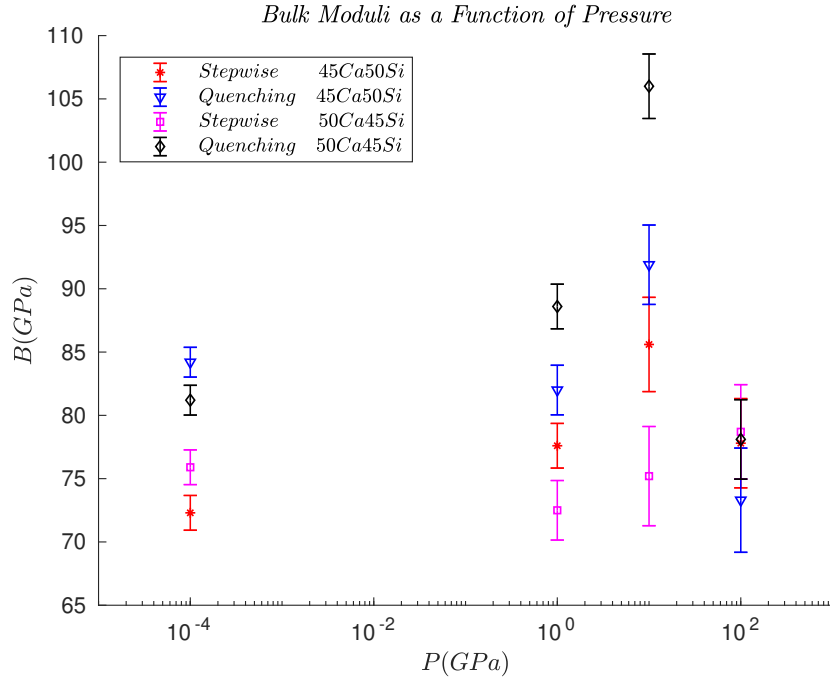


**Figure 5.19.** Bulk modulus as a function of pressure along with 95% confidence intervals is shown for the large system size of  $\approx 4000$  atoms for the two simulation methods Stepwise and Quenching for both 45Ca50Si and 50Ca45Si as indicated by the legend.

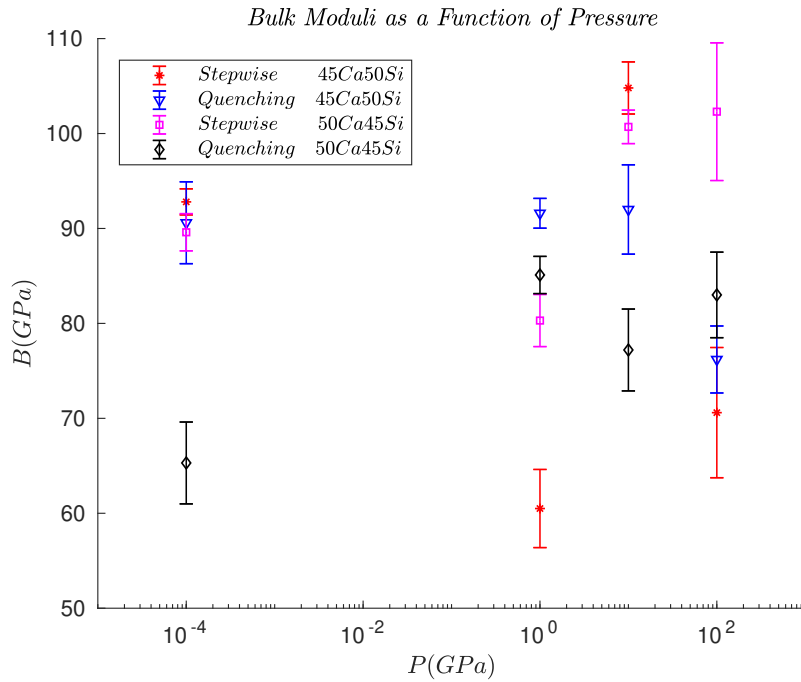


**Figure 5.20.** Bulk modulus as a function of pressure along with 95% confidence intervals is shown for the small system size of  $\approx 500$  atoms for the two simulation methods Stepwise and Quenching for both 45Ca50Si and 50Ca45Si as indicated by the legend.

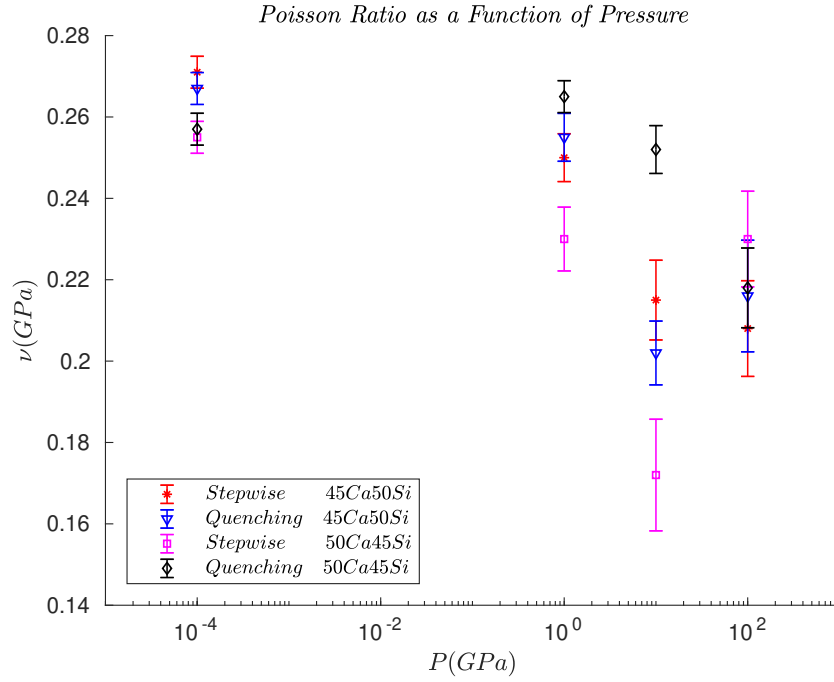


**Figure 5.21.** Poisson's ratio as a function of pressure along with 95% confidence intervals is shown for the large system size of  $\approx 4000$  atoms for the two simulation methods Stepwise and Quenching for both 45Ca50Si and 50Ca45Si as indicated by the legend.

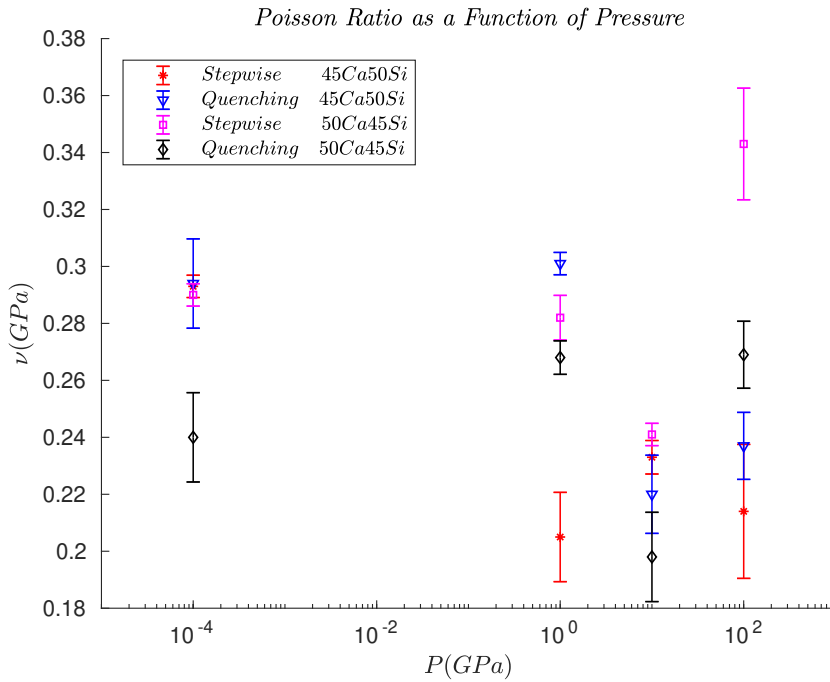


**Figure 5.22.** Poisson's ratio as a function of pressure along with 95% confidence intervals is shown for the large system size of  $\approx 500$  atoms for the two simulation methods Stepwise and Quenching for both 45Ca50Si and 50Ca45Si as indicated by the legend.

# Discussion 6

---

The precision and capability of the MD simulations to reproduce experimental data could be improved in several ways. The size effect is seen to have some effect going from a system size of  $\approx 4000$  to  $\approx 500$  for the two compositions and the different methods. Especially the Zr shows high sensibility when going from the large system to the small system size because the amount of Zr becomes too small to be statistically significant. Furthermore a system size larger than 4000atoms would also be appreciable for all off the RDF and CN numbers for Zr, Ca and Si to distinguish the different methods and compositions from each other.

The CN determination was done by selecting the bin from the LAMMPS data at the minimum after the peak. This could be improved by integration of the RDF ( $g(r)$ ) instead. Furthermore it might be even more precise if the integration is only done to the maximum of the peak because it is easier to detect and then multiplied by two assuming an even distribution.

The precision of the MD simulations for statistical averaging could also be improved with smaller timesteps, better damping off the temperature, longer runs, cut off and a tuning of the potential.

Both smaller timesteps, larger system size, cut off and longer runs would increase the duration of the simulation in real time but changing all of these parameters would inevitably improve the precision of the simulation results.

The cooling rate effect could be present in the small systems due to a size of  $\approx 500atoms$  but the deviation of the different parameters from experiment is not hugher than the deviation for the large system. The density is more or less over estimated for all of the runs except 3 out of 16 indicating that the cooling rate should be higher to reproduce the density properly.

If the small systems simulation cell size( $\approx 19\text{\AA}$ ) is compared with the cut off (8-10 $\text{\AA}$ ) it is seen that almost all the atoms behave as they were surface atoms whereas in the large system a part of them will actually behave as bulk material. This could affect the different elastic moduli and in the end the poisson ratio.

The role of calcium in the network is crucial to a lot of physical parameters for example the connectivity and  $T_g$  is affected. The role of Ca in Ca-aluminosilicate glasses has been investigated and concluded that that calciums role as either network modifier or charge compensator was linked to the degree of polymerisation. If the glass was highly polymerized(high connectivity) the role was charge compensator and not network modifier. [Cicconi et al., 2016]

In another study the glasses has been subjected to pressure and the role of calcium up to 8GPa has been investigated and is in good agreement with the above statement. It was found that the role of the calcium in the Ca-aluminosilicate glasses changed when the pressure went above  $\approx 3 - 4GPa$  from network modifier to charge compensator. This was due to the pressure induced increase in both the coordination number of Si and Al and thereby also the connectivity(decrease in NBO).[Lee, 2010]

In this study the CN of Si and Zr is plotted in figur 5.9 and 5.11 and seen to increase from respectively  $\approx 4.0$  and  $\approx 5.3$  to  $\approx 5.3$  and  $\approx 6.5$  which indicates the change of cations role from network modifier to charge compensator for both Si-O-Si and Zr-O-Zr sites. This statement could be supported in the increase off the coordination number for Ca from around  $\approx 4.6$  to  $\approx 7.6$  because it has to charge compensate both the Si and Zr sites.

This would give rise to an increase in connectivity followed by a drop in poisson's ratio if the pressure is above  $\approx 3 - 4GPa$  due to the change of the structural role of calcium.

The study off multicomponent glass at ultra high pressures up to 100GPa is not that common but there are some studies on single component glasses. Silica has been investigated up to 172GPa with the use off high-energy X-ray diffraction and both the average interatomic distance and CN was evaluated. The CN for Si remained constant at  $\approx 4$  up to 14GPa and then rose sharply to  $\approx 6$  at 40GPa and above 40GPa the CN shows a linearly increase up to  $\approx 7$  at a pressure of 172GPa. The Si-O interatomic distance remains constant at  $\approx 1.62$  up to 10GPa where it increases nearly linearly to  $\approx 1.69$  at 40GPa. Above the 40GPa the Si-O distance shows a linear decrease to 1.65 at 172GPa. The constant CN and Si-O distance at low pressures up to respectively 10GPa and 14GPa is due to the collapsing of void space in the amorphous structure. Then the interatomic distance increases from 10GPa to 40GPa due to the sharp increment in the CN between 14GPa and up to 40GPa. When the rate  $\frac{\partial CN}{\partial P}$  above 40GPa decreases and the increment in CN with respect to pressure becomes small the compression dominates and leads to the linearly decrease in Si-O distance.[Prescher et al.]

As shown in the figures 5.7, 5.9 and 5.11 the trend for Ca, Si and Zr is a constant value of CN up to 1GPa followed by a small increase up to 10GPa and then a rather high change in CN up to 100GPa. It is plausible that the trend between 10GPa and 100GPa could be the same as in the article [Prescher et al.] which could be shown by obtaining more measurements in this pressure regime 10GPa to 100GPa.

The Si-O distances shown in figure 5.3 could follow the trend mentioned above from article [Prescher et al.] with the trend between 10GPa and 100GPa not shown due to the lack of data. The Ca-O distance in figure 5.1 seems to follow the trend off Si-O up to 10GPa where it drops rather dramatically to an average interatomic distance below the starting point at 1atm. This could be explained by the pressure domination mentioned above from 40GPa and up that could lead to a larger decrease in the Ca-O distance than the Si-O. This could be due to the nature of Ca where it do not participate in the network formation at ultra high pressures but only charge compensates and thereby is more easily squeezed into small space in the network. The Zr-O distance show in figure 5.5 could follow the same trend as Si-O just explained above.

The pressure induced increase in density counteracts the effect of the increased connectivity by an increase in poisson's ratio. The competition between these two effects could possibly be seen in figure 5.21 for the Poisson ratio as a function of pressure. The poisson ratio shows a rather large decrease from 1GPa to 10GPa which could be explained by

the domination of the increasing connectivity at high pressure. Then the development from 10GPa to 100GPa is not that obvious some but it could be a plausible explanation that the density increase starts to dominate and increases the poisson ratio. The domain beyond 100GPa would be interesting to investigate due to this argument but maybe it is not possible to compress the glass enough to actually regain a poisson ratio as high as before pressurizing the glass.

As seen there is an over estimation of the stiffness matrix elements  $C_{11}$  and  $C_{44}$  which was estimated at 0Pa and 0K in the simulations. First of all the internal stress was not completely removed leaving a residual stress contributing to the elastic moduli and secondly the 0K corresponds to a static situation with no kinetic energy and hence no net movement of the atoms which is different from a dynamic situation at 300K where the atomic movements is more flexible. The more flexible movement off the atoms could lead to a decrease in both bulk, shear and Young's modulus.

In the articles [Manghnani, 1972], [Yu et al., 2007] and [Rajendran et al., 2002] it has been shown that the elastic moduli turned out to decrease significantly when the temperature was increased. For the multi-component oxide glasses in [Manghnani, 1972] and [Rajendran et al., 2002] the different moduli do not decrease with the same relative amount. The percentage increase of the elastic moduli for the glass compositions used in this study is hard to tell but for example the change was estimated to be  $\frac{dK}{dT} \approx -0.08 \frac{kbar}{K}$  and  $\frac{dG}{dT} \approx -0.07 \frac{kbar}{K}$  for one of the compositions in [Manghnani, 1972] which used in this study would lead to an increase in the elastic moduli going from 300K to 0K of  $\approx 3,5\%$  and  $\approx 5,5\%$  contributing to the over estimation of the elastic moduli.

The approximation for the stiffness matrix assumes that the glass obtained from the simulation is amorphous or isotropic. If the full stiffness matrix with no approximations was simulated the elements would reveal the symmetri requirements nescessary for isotropic behaviour. Applying the Voigt and Reuss equations should give the same results for isotropic materials and could be used as a test of how amorphous the glass actually is. [Xiang et al., 2013]

No matter how amorphous the material are it is still an approximation and to simulate the full stiffness matrix could improve the precision of the simulation results.



# Conclusion 7

---

It was not possible in general due to the lack of precision in the simulations to actually distinguish the different methods and compositions from each other when estimating the physical parameters though the Stepwise procedure with 4080atoms for  $45\text{Ca}50\text{Si}$  was clearly better at ambient pressure to estimate the density, stiffness matrix elements, elastic moduli and the Poisson ratio with respect to experimental data. Tuning of the Poisson ratio was not achieved and actually decreased during the pressurizing of the glass so another way to enhance the Poisson ratio must be advised.



# Bibliography

---

- Barbieri, Cannillo, Leonelli, Montorsi, Siligardi, og Mustarelli, 2015.** L. Barbieri, V. Cannillo, C. Leonelli, M. Montorsi, C. Siligardi, og P. Mustarelli. *Characterisation of CaO – ZrO<sub>2</sub> – SiO<sub>2</sub> glasses by MAS-NMR and molecular dynamics*. Phys. Chem. Glasses., 143, 2015.
- Bauchy, 2014.** M. Bauchy. *Structural, vibrational, and elastic properties of a calcium aluminosilicate glass from molecular dynamics simulations: The role of the potential*. J. Chem. Phys., 141, 2014.
- Cicconi, Ligny, Gallo, og Neuville, 2016.** Maria Rita Cicconi, Dominique de Ligny, Tamires M. Gallo, og Daniel R. Neuville. *Ca neighbors from XANES spectroscopy: A tool to investigate structure, redox, and nucleation processes in silicate glasses, melts, and crystals*. American Mineralogist, 101, 2016.
- Greaves, Greer, Lakes, og Rouxel, 2011.** G. N. Greaves, A. L. Greer, R. S. Lakes, og T. Rouxel. *Poisson's ratio and modern materials*. Nature Materials, 10, 2011.
- Lee, 2010.** Sung Keun Lee. *Effect of pressure on structure of oxide glasses at high pressure: Insights from solid-state NMR of quadrupolar nuclides*. Solid State Nuclear Magnetic Resonance, 38, 2010.
- Manghnani, 1972.** Murli H. Manghnani. *Pressure and Temperature Dependence of the Elastic Moduli of Na<sub>2</sub>O – TiO<sub>2</sub> – SiO<sub>2</sub>*. Journal of The American Ceramic Society, 55, 1972.
- Massobrio, Du, Bernasconi, og Salmon, 2015.** Carlo Massobrio, Jincheng Du, Marco Bernasconi, og Philip S. Salmon. *Molecular Dynamics Simulations of Disordered Materials From Network Glasses to Phase-Change Memory Alloys*, volume 215. Springer, 2015.
- Montorsi, Leonelli, Menziani, Cormack, og Cormack, 2002.** M. Montorsi, C. Leonelli, M. C. Menziani, J. Du. Cormack, og A. N. Cormack. *Molecular dynamics study of zirconia containing glasses*. Phys. Chem. Glasses., 43, 2002.
- Prescher, Prakapenka, Stefanski, Jahn, Skinner, og Wang.** Clemens Prescher, Vitali B. Prakapenka, Johannes Stefanski, Sandro Jahn, Lawrie B. Skinner, og Yanbin Wang. *Beyond sixfold coordinated Si in SiO<sub>2</sub>*.
- Rajendran, Begum, Azooz, og Batal, 2002.** V. Rajendran, A. Nishara Begum, M. A. Azooz, og F. H. El Batal. *Microstructural dependence on relevant*

*physical-mechanical properties on  $\text{SiO}_2 - \text{Na}_2\text{O} - \text{CaO} - \text{P}_2\text{O}_5$  biological glasses.* Biomaterials, 23, 2002.

**Shi, Luo, Yuan, og Huang, 2014.** Yunfeng Shi, Jian Luo, Fenglin Yuan, og Liping Huang. *Intrinsic ductility of glassy solids.* J. Appl. Phys., 115, 2014.

**Tilocca, 2013.** Antonio Tilocca. *Cooling rate and size effects on the medium-range structure of multicomponent oxide glasses simulated by molecular dynamics.* J. Chem. Phys., 139, 2013.

**Xiang, Du, Smedskjaer, og Mauro, 2013.** Ye Xiang, Jincheng Du, Morten M. Smedskjaer, og John C. Mauro. *Structure and properties of sodium aluminosilicate glasses from molecular dynamics simulations.* J. Chem. Phys., 139, 2013.

**Yu, Wang, Zhao, og Bai, 2007.** Peng Yu, R. J. Wang, D. Q. Zhao, og H. Y. Bai. *Temperature dependence of elastic moduli in bulk metallic glasses down to liquid nitrogen temperature.* Appl. Phys. Lett, 90, 2007.

# Tables A

## A.1 RDF and CN

Pressure	Average Interatomic Distances			Coordination Number		
	Ca-O	Si-O	Zr-O	Ca	Si	Zr
1atm	2,37	1,60	1,98-2,02	6,15	4,00	5,30

**Table A.1.** Experimental data for the average interatomic distances and the coordination number taken from the source [Montorsi et al., 2002] and is used to compare with the simulation data.

	Pressure	Average Interatomic Distances			Coordination Number		
		Ca-O	Si-O	Zr-O	Ca	Si	Zr
Stepwise 4080 Atoms	1atm	$2,081 \pm 0,006$	$1,574 \pm 0,001$	$1,957 \pm 0,004$	4,48	4,03	5,21
	1GPa	$2,091 \pm 0,007$	$1,573 \pm 0,001$	$1,970 \pm 0,006$	4,71	4,06	5,34
	10GPa	$2,116 \pm 0,011$	$1,581 \pm 0,005$	$1,991 \pm 0,005$	5,78	4,36	6,12
	100GPa	$2,023 \pm 0,011$	$1,649 \pm 0,006$	$1,957 \pm 0,009$	7,73	5,18	6,42
Stepwise 510 Atoms	1atm	$2,090 \pm 0,007$	$1,573 \pm 0,001$	$2,013 \pm 0,003$	4,54	4,08	5,54
	1GPa	$2,088 \pm 0,008$	$1,573 \pm 0,001$	$1,955 \pm 0,004$	4,69	4,05	5,31
	10GPa	$2,116 \pm 0,008$	$1,583 \pm 0,004$	$1,994 \pm 0,007$	5,72	4,35	5,96
	100GPa	$2,035 \pm 0,011$	$1,662 \pm 0,007$	$1,984 \pm 0,010$	7,74	5,46	6,79
Quenching 4080 Atoms	1atm	$2,091 \pm 0,006$	$1,573 \pm 0,001$	$1,974 \pm 0,005$	4,60	4,03	5,38
	1GPa	$2,097 \pm 0,007$	$1,573 \pm 0,001$	$1,986 \pm 0,004$	4,82	4,06	5,52
	10GPa	$2,125 \pm 0,011$	$1,581 \pm 0,005$	$1,996 \pm 0,005$	5,92	4,42	6,13
	100GPa	$2,023 \pm 0,012$	$1,651 \pm 0,006$	$1,961 \pm 0,010$	7,71	5,44	6,08
Quenching 510 Atoms	1atm	$2,101 \pm 0,006$	$1,573 \pm 0,001$	$1,949 \pm 0,005$	4,61	4,01	5,26
	1GPa	$2,096 \pm 0,007$	$1,571 \pm 0,001$	$1,992 \pm 0,006$	4,69	4,04	5,50
	10GPa	$2,133 \pm 0,012$	$1,590 \pm 0,006$	$2,004 \pm 0,003$	6,09	4,38	5,84
	100GPa	$2,026 \pm 0,011$	$1,661 \pm 0,008$	$1,936 \pm 0,010$	7,67	5,28	5,41

**Table A.2.** Average interatomic distances and coordination number from the simulations of  $45CaO - 5ZrO_2 - 50SiO_2$  through both Stepwise and Quenching methods on two different system sizes (4080 and 510) with the standard deviation given for all of the average interatomic distances.

		Average Interatomic Distances			Coordination Number		
Pressure		Ca-O	Si-O	Zr-O	Ca	Si	Zr
Stepwise 4000 Atoms	1atm	2,089 ± 0,006	1,571 ± 0,001	1,966 ± 0,004	4,64	4,06	5,31
	1GPa	2,092 ± 0,007	1,571 ± 0,001	1,980 ± 0,004	4,77	4,07	5,45
	10GPa	2,111 ± 0,010	1,581 ± 0,005	2,000 ± 0,004	5,80	4,40	6,16
	100GPa	2,017 ± 0,011	1,653 ± 0,006	1,962 ± 0,010	7,61	5,25	7,09
Stepwise 500 Atoms	1atm	2,086 ± 0,006	1,572 ± 0,001	2,008 ± 0,006	4,59	4,04	5,60
	1GPa	2,090 ± 0,007	1,569 ± 0,001	1,946 ± 0,005	4,67	4,02	5,48
	10GPa	2,102 ± 0,008	1,577 ± 0,003	1,972 ± 0,007	5,57	4,28	6,20
	100GPa	2,008 ± 0,011	1,669 ± 0,005	1,940 ± 0,013	7,59	5,68	6,85
Quenching 4000 Atoms	1atm	2,090 ± 0,006	1,571 ± 0,001	1,980 ± 0,004	4,60	4,03	5,38
	1GPa	2,098 ± 0,008	1,570 ± 0,001	2,007 ± 0,005	4,89	4,06	5,72
	10GPa	2,116 ± 0,010	1,577 ± 0,004	2,000 ± 0,003	5,85	4,35	6,15
	100GPa	2,018 ± 0,012	1,658 ± 0,006	1,966 ± 0,010	7,65	5,26	6,48
Quenching 500 Atoms	1atm	2,090 ± 0,006	1,573 ± 0,001	1,963 ± 0,004	4,67	4,03	5,31
	1GPa	2,088 ± 0,008	1,571 ± 0,001	1,953 ± 0,003	4,90	4,09	5,31
	10GPa	2,100 ± 0,010	1,582 ± 0,005	1,988 ± 0,004	5,74	4,45	5,66
	100GPa	2,018 ± 0,010	1,660 ± 0,005	1,975 ± 0,010	7,49	5,26	6,60

**Table A.3.** Average interatomic distances and coordination number from the simulations of  $50CaO - 5ZrO_2 - 45SiO_2$  through both Stepwise and Quenching methods on two different system sizes (4000 and 500) with the standard deviation given for all of the average interatomic distances.

## A.2 Density, Stiffness matrix elements, Elastic Modulus and Poisson's Ratio

Pressure		$\rho$	$C_{11}$	$C_{44}$	$C_{12}$	$E$	$G$	$B$	$\nu$
Stepwise 4080 Atoms	1atm	2,887 ± 0,001	124,5 ± 0,6	39,1 ± 0,3	46,2 ± 0,9	99,4 ± 0,6	39,1 ± 0,3	72,3 ± 0,7	0,271 ± 0,002
	1GPa	3,085 ± 0,001	139,6 ± 0,8	46,5 ± 0,3	46,6 ± 0,9	116,2 ± 0,5	46,5 ± 0,3	77,6 ± 0,9	0,250 ± 0,003
	10GPa	3,810 ± 0,001	165,9 ± 1,8	60,2 ± 0,5	45,4 ± 2,0	146,4 ± 0,9	60,2 ± 0,5	85,6 ± 1,9	0,215 ± 0,005
	100GPa	5,105 ± 0,001	153,1 ± 1,6	56,5 ± 0,5	40,2 ± 1,9	136,4 ± 1,0	56,5 ± 0,5	77,8 ± 1,8	0,208 ± 0,006
Stepwise 510 Atoms	1atm	2,988 ± 0,003	152,2 ± 0,5	44,6 ± 0,4	63,1 ± 0,9	115,2 ± 0,7	44,6 ± 0,4	92,8 ± 0,7	0,293 ± 0,002
	1GPa	3,100 ± 0,003	119,8 ± 2,0	44,5 ± 0,5	30,8 ± 2,2	107,1 ± 1,1	44,5 ± 0,5	60,5 ± 2,1	0,205 ± 0,008
	10GPa	3,836 ± 0,005	195,6 ± 1,2	68,1 ± 0,5	59,4 ± 1,6	168,0 ± 0,9	68,1 ± 0,5	104,8 ± 1,4	0,233 ± 0,003
	100GPa	5,121 ± 0,002	137,1 ± 3,0	49,9 ± 1,3	37,4 ± 4,0	121,1 ± 2,2	49,9 ± 1,3	70,6 ± 3,5	0,214 ± 0,012
Quenching 4080 Atoms	1atm	2,966 ± 0,001	146,0 ± 0,5	46,3 ± 0,3	53,3 ± 0,7	117,5 ± 0,5	46,3 ± 0,3	84,2 ± 0,6	0,267 ± 0,002
	1GPa	3,149 ± 0,001	145,8 ± 0,9	47,9 ± 0,3	50,0 ± 1,1	120,3 ± 0,6	47,9 ± 0,3	82,0 ± 1,0	0,255 ± 0,003
	10GPa	3,845 ± 0,001	182,9 ± 1,5	68,3 ± 0,4	46,3 ± 1,7	164,2 ± 0,8	68,3 ± 0,4	91,9 ± 1,6	0,202 ± 0,004
	100GPa	5,115 ± 0,001	141,6 ± 2,0	51,3 ± 0,5	39,1 ± 2,2	124,7 ± 1,0	51,3 ± 0,5	73,3 ± 2,1	0,216 ± 0,007
Quenching 510 Atoms	1atm	2,931 ± 0,001	148,1 ± 0,9	43,2 ± 1,5	61,8 ± 3,2	111,7 ± 3,1	43,2 ± 1,5	90,6 ± 2,2	0,294 ± 0,008
	1GPa	3,076 ± 0,001	147,9 ± 0,7	42,2 ± 0,4	63,5 ± 1,0	109,7 ± 0,8	42,2 ± 0,4	91,6 ± 0,8	0,301 ± 0,002
	10GPa	3,871 ± 0,002	176,4 ± 2,0	63,3 ± 1,0	49,8 ± 2,9	154,5 ± 1,7	63,3 ± 1,0	92,0 ± 2,4	0,220 ± 0,007
	100GPa	5,122 ± 0,004	140,8 ± 1,7	48,5 ± 0,5	43,9 ± 2,0	120,0 ± 0,9	48,5 ± 0,5	76,2 ± 1,8	0,237 ± 0,006

**Table A.4.** The results for density( $\rho$ ), stiffness matrix elements( $C_{11}$ ,  $C_{44}$  and  $C_{12}$ ), Youngs moduli( $E$ ), Shear moduli( $G$ ), Bulk moduli( $B$ ) and Poisson's ratio( $\nu$ ) is shown for the different pressures (1atm, 1GPa, 10GPa and 100GPa) along with their standard deviation for the composition  $45CaO - 5ZrO_2 - 50SiO_2$  and different methods and system sizes.

	Pressure	$\rho$	$C_{11}$	$C_{44}$	$C_{12}$	$E$	$G$	$B$	$\nu$
Stepwise 4000 Atoms	1atm	$3,047 \pm 0,001$	$135,1 \pm 0,6$	$44,4 \pm 0,3$	$46,3 \pm 0,8$	$111,4 \pm 0,5$	$44,4 \pm 0,3$	$75,9 \pm 0,7$	$0,255 \pm 0,002$
	1GPa	$3,208 \pm 0,001$	$136,2 \pm 1,1$	$47,8 \pm 0,4$	$40,7 \pm 1,4$	$117,5 \pm 0,7$	$47,8 \pm 0,4$	$72,5 \pm 1,2$	$0,230 \pm 0,004$
	10GPa	$3,882 \pm 0,001$	$159,6 \pm 2,0$	$63,3 \pm 0,4$	$33,1 \pm 2,1$	$148,2 \pm 1,0$	$63,3 \pm 0,4$	$75,2 \pm 2,0$	$0,172 \pm 0,007$
	100GPa	$5,173 \pm 0,001$	$147,9 \pm 1,7$	$51,9 \pm 0,7$	$44,1 \pm 2,1$	$127,6 \pm 1,2$	$51,9 \pm 0,7$	$78,7 \pm 1,9$	$0,230 \pm 0,006$
Stepwise 500 Atoms	1atm	$3,031 \pm 0,003$	$147,9 \pm 0,8$	$43,7 \pm 0,4$	$60,4 \pm 1,1$	$112,8 \pm 0,7$	$43,7 \pm 0,4$	$89,6 \pm 1,0$	$0,290 \pm 0,002$
	1GPa	$3,180 \pm 0,005$	$134,9 \pm 1,3$	$40,9 \pm 0,5$	$53,1 \pm 1,6$	$105,0 \pm 1,0$	$40,9 \pm 0,5$	$80,3 \pm 1,4$	$0,282 \pm 0,004$
	10GPa	$3,819 \pm 0,003$	$184,9 \pm 0,9$	$63,1 \pm 0,2$	$58,7 \pm 0,9$	$156,6 \pm 0,4$	$63,1 \pm 0,2$	$100,7 \pm 0,9$	$0,241 \pm 0,002$
	100GPa	$5,174 \pm 0,002$	$150,0 \pm 2,1$	$35,8 \pm 2,2$	$78,4 \pm 5,0$	$96,2 \pm 5,1$	$35,8 \pm 2,2$	$102,3 \pm 3,7$	$0,343 \pm 0,010$
Quenching 4000 Atoms	1atm	$3,030 \pm 0,001$	$144,1 \pm 0,5$	$47,1 \pm 0,3$	$49,8 \pm 0,7$	$118,5 \pm 0,5$	$47,1 \pm 0,3$	$81,2 \pm 0,6$	$0,257 \pm 0,002$
	1GPa	$3,240 \pm 0,001$	$154,4 \pm 0,8$	$49,3 \pm 0,3$	$55,7 \pm 1,0$	$124,8 \pm 0,6$	$49,3 \pm 0,3$	$88,6 \pm 0,9$	$0,265 \pm 0,002$
	10GPa	$3,884 \pm 0,001$	$190,2 \pm 1,3$	$63,1 \pm 0,3$	$63,9 \pm 1,4$	$158,0 \pm 0,5$	$63,1 \pm 0,3$	$106,0 \pm 1,3$	$0,252 \pm 0,003$
	100GPa	$5,185 \pm 0,001$	$150,5 \pm 1,5$	$54,3 \pm 0,4$	$41,8 \pm 1,7$	$132,3 \pm 0,7$	$54,3 \pm 0,4$	$78,1 \pm 1,6$	$0,218 \pm 0,005$
Quenching 500 Atoms	1atm	$3,064 \pm 0,003$	$120,1 \pm 1,8$	$41,1 \pm 0,9$	$38,0 \pm 2,6$	$101,8 \pm 1,6$	$41,1 \pm 0,9$	$65,3 \pm 2,2$	$0,240 \pm 0,008$
	1GPa	$3,198 \pm 0,004$	$147,3 \pm 0,8$	$46,7 \pm 0,5$	$54,0 \pm 1,3$	$118,3 \pm 1,0$	$46,7 \pm 0,5$	$85,1 \pm 1,0$	$0,268 \pm 0,003$
	10GPa	$3,868 \pm 0,002$	$155,1 \pm 1,5$	$58,4 \pm 1,2$	$38,3 \pm 2,9$	$140,0 \pm 1,8$	$58,4 \pm 1,2$	$77,2 \pm 2,2$	$0,198 \pm 0,008$
	100GPa	$5,188 \pm 0,004$	$143,4 \pm 2,1$	$45,3 \pm 0,6$	$52,8 \pm 2,5$	$115,0 \pm 1,3$	$45,3 \pm 0,6$	$83,0 \pm 2,3$	$0,269 \pm 0,006$

**Table A.5.** The results for density( $\rho$ ), stiffness matrix elements( $C_{11}$ ,  $C_{44}$  and  $C_{12}$ ), Youngs moduli( $E$ ), Shear moduli( $G$ ), Bulk moduli( $B$ ) and Poisson's ratio( $\nu$ ) is shown for the different pressures (1atm, 1GPa, 10GPa and 100GPa) along with their standard deviation for the composition  $50CaO - 5ZrO_2 - 45SiO_2$  and different methods and system sizes.

Pressure	$\rho$	$C_{11}$	$C_{44}$	$C_{12}$	$E$	$G$	$B$	$\nu$
1atm	$2,968 \pm 0,003$	$115,8 \pm 0,2$	$35,9 \pm 0,6$	$43,9 \pm 1,2$	$91,7 \pm 1,2$	$35,9 \pm 0,6$	$67,8 \pm 0,8$	$0,275 \pm 0,004$
1GPa	$3,001 \pm 0,003$	$118,4 \pm 0,2$	$36,6 \pm 0,6$	$45,1 \pm 1,2$	$93,5 \pm 1,2$	$36,6 \pm 0,6$	$69,5 \pm 0,8$	$0,276 \pm 0,004$

**Table A.6.** The results for density( $\rho$ ), stiffness matrix elements( $C_{11}$ ,  $C_{44}$  and  $C_{12}$ ), Youngs moduli( $E$ ), Shear moduli( $G$ ), Bulk moduli( $B$ ) and Poisson's ratio( $\nu$ ) is shown for the different pressures (1atm and 1GPa) along with their standard deviation for the composition  $45CaO - 5ZrO_2 - 50SiO_2$ .

Pressure	$\rho$	$C_{11}$	$C_{44}$	$C_{12}$	$E$	$G$	$B$	$\nu$
1atm	$3,005 \pm 0,016$	$113,1 \pm 0,2$	$33,7 \pm 0,6$	$45,7 \pm 1,2$	$86,8 \pm 1,2$	$33,7 \pm 0,6$	$68,1 \pm 0,8$	$0,288 \pm 0,004$
1GPa	$3,032 \pm 0,003$	$116,2 \pm 0,2$	$35,7 \pm 0,6$	$44,8 \pm 1,2$	$91,2 \pm 1,2$	$35,7 \pm 0,6$	$68,6 \pm 0,8$	$0,278 \pm 0,004$

**Table A.7.** The results for density( $\rho$ ), stiffness matrix elements( $C_{11}$ ,  $C_{44}$  and  $C_{12}$ ), Youngs moduli( $E$ ), Shear moduli( $G$ ), Bulk moduli( $B$ ) and Poisson's ratio( $\nu$ ) is shown for the different pressures (1atm and 1GPa) along with their standard deviation for the composition  $50CaO - 5ZrO_2 - 45SiO_2$ .

### A.3 LAMMPS Code